Geoscience Frontiers 14 (2023) 101654

Contents lists available at ScienceDirect

Geoscience Frontiers

journal homepage: www.elsevier.com/locate/gsf

Research Paper

Crustal architecture and metallogeny associated with the Paleo-Tethys evolution in the Eastern Kunlun Orogenic Belt, Northern Tibetan Plateau

Xinming Zhang [a,b], Xu Zhao [a,c,*], Lebing Fu [a], Yanjun Li [a], Andreas Kamradt [b], M. Santosh [d,e], Chongwen Xu [a], Xiaokun Huang [a], Gregor Borg [b], Junhao Wei [a]

[a] School of Earth Resource, China University of Geoscience, Wuhan 430074, China
[b] Institute of Geosciences and Geography, Martin Luther University Halle-Wittenberg, Halle (Saale) 06120, Germany
[c] CAS Key Laboratory of Mineralogy and Metallogeny/Guangdong Provincial Key Laboratory of Mineral Physics and Materials, Guangzhou Institute of Geochemistry, Chinese Academy of Sciences, Guangzhou 510640, China
[d] School of Earth Science and Resources, China University of Geosciences, Beijing 100083, China
[e] Department of Earth Sciences, University of Adelaide, Adelaide, SA 5005, Australia

ARTICLE INFO

Article history:
Received 17 December 2022
Revised 24 March 2023
Accepted 20 June 2023
Available online 23 June 2023
Handling Editor: C. Manikyamba

Keywords:
Hf-isotopic mapping
Crustal thickness
Metallogeny
Tectonic evolution
Crustal architecture
Eastern Kunlun Orogenic Belt

ABSTRACT

The Eastern Kunlun Orogenic Belt (EKOB) in the Northern Tibet Plateau hosts a wide variety of metal deposits related to the Late Paleozoic to Mesozoic magmatism. In this study, we investigate the spatio-temporal distribution of the Late Paleozoic to Mesozoic granitic rocks and associated metal deposits in the EKOB and provide a comprehensive compilation of the geochronological, geochemical and isotopic data on these rocks. We compute regional zircon Hf isotope and crustal thickness maps from the data, based on which a comprehensive model is proposed involving subduction (ca. 270–240 Ma), continental collision (ca. 240–224 Ma), and post-collisional extension (ca. 224–200 Ma) for the Late Paleozoic to Mesozoic Paleo-Tethys evolution in the EKOB.

Zircon Hf isotopic and crustal thickness mapping of Late Paleozoic to Mesozoic magmatic rocks was carried out to evaluate their spatio-temporal and genetic links with the regional metallogeny. The polymetallic Fe-skarn and porphyry Cu (Mo) deposits in the EKOB are located above the Moho uplift region, featuring a comparatively thin crust. Granites associated with porphyry Cu (Mo) and polymetallic Fe skarn mineralization are commonly characterized by high $\varepsilon_{Hf}(t)$ and younger T_{DM}c values, whereas granite related to Cu-Mo-Sn skarn deposits exhibit more variable $\varepsilon_{Hf}(t)$ values, T_{DM}c ages, and the crust thickness, which suggest that more crustal materials contributed to the formation of Cu-Mo-Sn skarn deposits than those for porphyry Cu (Mo) and polymetallic Fe skarn mineralization. In contrast, vein-type Au deposits are located primarily where the Moho surface displays a depression, i.e., where the continental crust is relatively thick. The magmatic rocks associated with Au mineralization are characterized by low $\varepsilon_{Hf}(t)$ and high T_{DM}c values, representing reworked ancient crustal components, similar to those associated with porphyry Mo and epithermal Ag-Pb-Zn-(Au) deposits. Our study indicates that the emplacement of magmatic-hydrothermal deposits was controlled by the crustal structure and magma sources.

1. Introduction

Plate tectonic processes exert a fundamental control on the formation of major ore deposits through time in Earth history (Bierlein et al., 2002; Goldfarb et al., 2005; Sillitoe, 2010; Santosh and Groves, 2022). In major orogenic belts, such as the Tibetan-Himalayan and Qinling in Central Asia, the Alps in Europe, as well as the Zagros belts in Iran, important base and precious metal deposits were generated throughout the entire orogenic cycle, from oceanic subduction to continental collision, and finally during post-collision extension (Sillitoe, 2008; Hou and Zhang, 2015; Richards, 2015; Deng et al., 2017). These orogens are well-endowed with abundant large and giant mineral deposits, including the well-known Yulong (China), Kounrad (Kazakhstan), Oyu Tolgoi (Mongolia), Kal'makyr and Arasbaran-Kerman (Uzbekistan), Mt. Emmons (American) porphyry deposits, Fierro skarn deposit and Imiter epithermal Ag deposit (Peru), and the

* Corresponding author at: Key Laboratory of Mineral Physics and Materials, Guangzhou Institute of Geochemistry, No. 511 Kehua Street, Tianhe District, Guangzhou 510640, China.

E-mail address: zhaoxu@gig.ac.cn (X. Zhao).

https://doi.org/10.1016/j.gsf.2023.101654
1674-9871/

Piranshahr-Saqez-Sardasht orogenic Au deposits (Iran) (Turner and Bowman, 1993; Morishita and Nakano, 2008; Hou et al., 2015; Richards, 2015; Wang et al., 2015; Wang et al., 2016a; Wu et al., 2021a). The general characteristics, spatial distribution, and timing of formation of these diverse types of metal deposits are closely related to the geodynamic framework of their host orogen (Bierlein et al., 2002; Groves and Santosh, 2021). Numerous metal deposit models have been established, such as the formation of orogenic Au deposits in accretionary wedges (Goldfarb et al., 2005), porphyry Cu and epithermal Au deposits in magmatic arcs (Sillitoe, 2010), volcanogenic massive sulfide (VMS) deposits in back-arc settings (Lydon, 1988; Franklin et al., 2005) and sediment-hosted Pb-Zn deposits within passive continental margin sequences (Leach et al., 2005). In addition to the particular tectonic settings and the geodynamic framework, the crustal architecture also controls the spatiotemporal distribution and genesis of these metal deposits (Hou and Zhang, 2015). For example, Nd-Hf isotope mapping studies of the West Yilgam Craton have suggested that the lithospheric discontinuities are enrichment areas for nickel, gold, and iron deposits. Nickel deposits are hosted in komatiites at the transition between young and ancient bodies and BIF-type iron ore deposits are found at the center and rims of old or remelted crust (Mole et al., 2014; Mole et al., 2019). The Hf isotope mapping studies of the Himalayan–Tibetan Orogen suggested that the porphyry Cu-Au deposits and Cu-Mo deposits are confined within the juvenile crust and the granite-related Pb-Zn deposits and porphyry Mo deposits are mainly produced within the ancient crust (Hou et al., 2015). Therefore, information about crustal architecture and its link to the mineralization and tectonic setting helps to improve the understanding of the origin and distribution of metal deposits and could provide a guide for regional exploration (Bierlein et al., 2006; Chen, 2013; Groves and Santosh, 2021).

The Eastern Kunlun Orogenic Belt (EKOB) is located in the northern region of the Tibetan Plateau and has received significant attention in terms of its orogenesis and metallogenesis during Permian to Triassic (Mo et al., 2007; Pan et al., 2012; Deng et al., 2017). Various metallic deposits, including porphyry-type Cu-Mo and Mo, skarn-type Fe and Cu-Mo-Sn, epithermal Ag-Pb-Zn-(Au), and vein-type Au deposits, induced by the subduction of the Paleo-Tethys Ocean, subsequent continental collision and post-collisional extension (Chen et al., 2020; Zhong et al., 2021; Guo et al., 2022), during which the crustal architecture was also influenced by the evolution of the Paleo-Tethys Ocean and may have a control to the ore generation (Zhang, 2012; Yao et al., 2017). Despite extensive research in the past, the spatio-temporal relationship between the crustal architecture and the formation of these metal deposits in the EKOB remain poorly understood. In this study, we compile a comprehensive geochemistry dataset related to magmatism rock during the evolution of the Paleo-Tethys in the EKOB. Specifically, our objectives are to: (1) constrain the spatio-temporal link between magmatism and metallogenesis of ore deposits in the EKOB, (2) evaluate the changes in tectonic activity and their spatial and genetic link to the crustal architecture, and (3) assess the role of the crustal architecture in controlling the generation of the metal deposits.

2. Geological setting

The EKOB is located in the western segment of the Central China Orogenic Belt (Fig. 1, Shao et al., 2017; Dong et al., 2018; Wu et al., 2019). The EKOB is limited by the Hongliuquan–Golmud fault (HGF) towards the northern Qaidam Block and the Muztagh-Buqingshan–Anemaqen ophiolitic melange zone (MBAM) towards the southern Bayanhar Terrane (Chen et al., 2012, 2017; Dong et al., 2022). It has undergone multiple episodes of orogeneses that correspond to the evolution of the Neoproterozoic to Early Paleozoic Proto-Tethys Ocean and Late Paleozoic to Mesozoic Paleo-Tethys Ocean (Bouilhol et al., 2013; Xiong et al., 2016; Zhao et al., 2022).

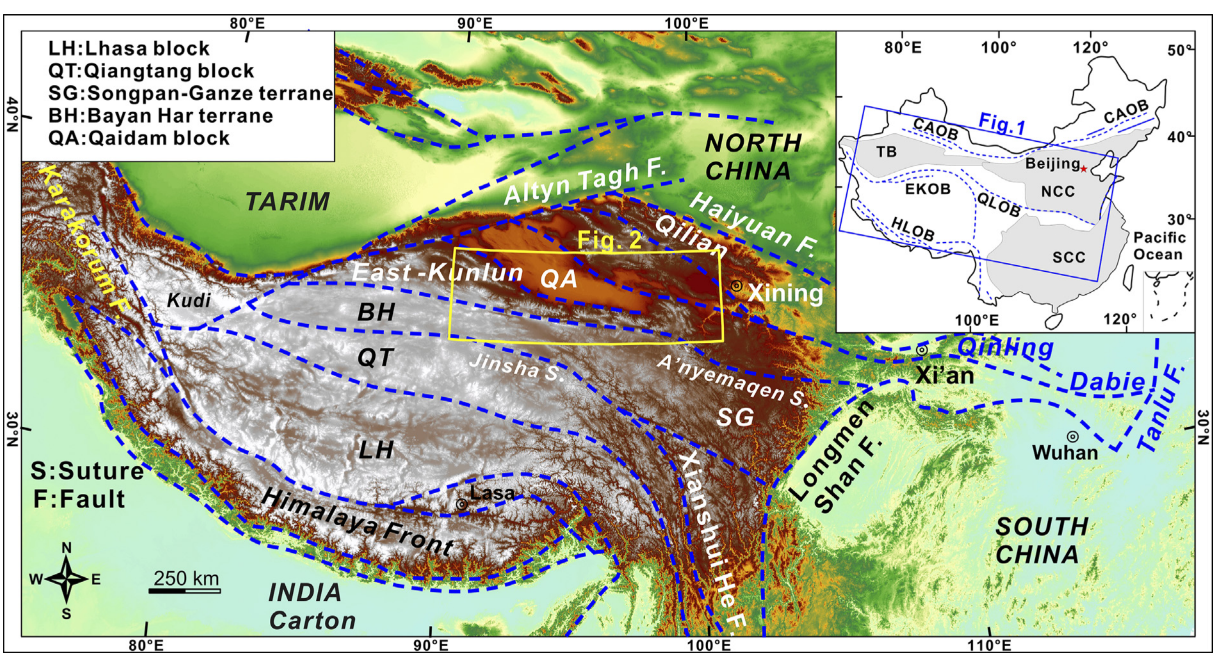

Fig. 1. Tectonic outline of the Tibetan Plateau showing the location of the East Kunlun Orogenic Belt (EKOB). Inset map shows location of the area within China (Deng et al., 2017; Zhao et al., 2022). CAOB = Central Asia Orogenic Belt, TB = Tarim Basin, EKOB = Eastern Kunlun Orogenic Belt, NCC = North China Craton, SCC = South China Craton, QLOB = Qinling Orogenic Belt, HLOB = Himalayan Orogenic Belt.

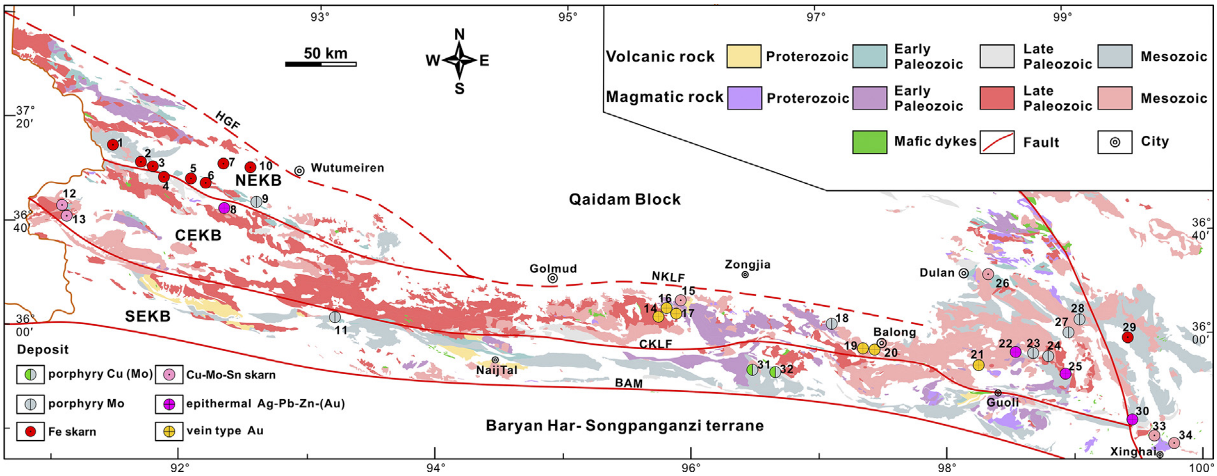

Fig. 2. Geologic map of the East Kunlun Orogen belt (Modified after Wu et al., 2021c; Dong et al., 2022). Geologic features of significant ore deposits labeled with numbers are listed in Table 2. BAM = Buqingshan–A'nyemaqen mélange zone; CEKB = Central Kunlun Belt; CKLF = Central Kunlun Fault; HGF = Hongliuquan–Golmud Fault; NEKB = Northern Eastern Kunlun Belt; NKLF = Northern Eastern Kunlun Fault; SEKB = South Eastern Kunlun Belt.

The EKOB is subdivided into three sections from north to south: i.e., the Northern, Central, and South Eastern Kunlun Belt from north to south. They are separated by the sinistral strike-slip faults of North Kunlun and Central Kunlun sutures (Fig. 2, Huang et al., 2014; Li et al., 2015a; He et al., 2016). Additionally, different subterranes are also characterized by specific sedimentary covers, magmatic groups, and metamorphic basements. Detailed information on these subterranes can be found in Table 1, Fig. 3 and Supplement Data Table S1. At least four principal types of ore deposits are recognized in the EKOB: (1) porphyry type Cu-Mo, Mo, (2) Fe-, and Cu-Mo-Sn skarn, (3) vein-type Au, and (4) epithermal Ag-Pb-Zn-(Au) polymetallic deposits. A summary of the geological distribution characteristics of these ore deposits is provided in Table 2, while the temporal distribution characteristics are illustrated in Fig. 4.

3. Data acquirement and visualization

3.1. Sampling strategy

Information and data of rock types, major and trace elements, particularly the elements related to crustal thickness estimations, U-Pb ages, Lu-Hf isotopic data of zircons, the latitude and longitude of the Late Paleozoic and Mesozoic magmatic rocks within the EKOB were systematically collected. Detailed information is provided in the Supplementary Data Tables to this publication.

3.2. Zircon Hf isotope data

From the original data (e.g., age, $^{176}Yb/^{177}Hf$, $^{176}Lu/^{177}Hf$, and $^{176}Hf/^{177}Hf$), we recalculated the values of $\varepsilon_{Hf}(0)$, $\varepsilon_{Hf}(t)$, $f_{Lu/Hf}$, T^{1}_{DM} and $T_{DM}c$ by using the same set of reference parameters and formulae described in Supplement Data Table S2. The $\varepsilon_{Hf}(t)$ notation was used to express the zircon Lu-Hf isotope data, which represents the deviation of the measured $^{176}Hf/^{177}Hf$ ratio from that of chondritic meteorites (CHUR) in parts per 10,000 (Wu et al., 2006). The juvenile and old continental crustal sources can be distinguished by their positive ε_{Hf} and negative ε_{Hf} values, respectively (Kemp et al., 2006). The crustal Hf model ages ($T_{DM}c$) estimate the age when the magmatic source was extracted from a depleted mantle reservoir (Griffin et al., 2002; Kemp et al., 2006). The use of the median for a range of zircon $\varepsilon_{Hf}(t)$ and $T_{DM}c$ values for individual samples helped to exclude the abnormal data. The summary of the median values can be found in Supplement Data Table S3.

3.3. Calculation of the crustal thickness

The EKOB is a typical continental collision orogen. Hence, the crustal thicknesses were calculated for this study using the model provided by Hu et al. (2017), which estimates the crustal thickness evolution of an orogen from oceanic subduction to continental collision.

The major and trace elements of the Late Paleozoic and Mesozoic magmatic rocks in the EKOB were collected and listed in the Supplementary Data Table S4. For all datasets, the samples with a relatively wider range of SiO_2 (55–72 wt.%) and MgO (0.5–6.0 wt.%) contents were selected, and the corresponding data can be found in the Supplementary Data Table S5. This silica range was used to eliminate mafic rocks, generated in the mantle and high silica granites. Subsequently, we removed Sr/Y and $(La/Yb)_N$ outliers from each data subset by using the modified Thompson tau statistical method. The data subsets with average Rb/Sr > 0.35 or with STD > 10 were discarded. Finally, we calculated the median Sr/Y and $(La/Yb)_N$ of each subset. The Rb/Sr filter was used to remove the samples that were strongly influenced by the fractionation within the crust. We eliminated high Sr/Y (average > 60) and high La (average > 60) from our data subsets due to their undefined petrogenesis with adakitic features. The selected and calculated results are listed in Supplementary Data Table S6 and S7, respectively.

3.4. Contour-mapping methods

Contour maps were produced using the ArcGIS software (ESRI) by the use of the inverse distance weighted interpolation method as described by Mole et al. (2014), Mole et al. (2019) and Webb et al. (2020). This method used 12 nearest neighbors at a "power" of 2 in the Geostatistical Analyst modeling feature of ArcGIS, which accounts for the distance between sample points in the most representative manner (Hou et al., 2015; Wang et al., 2017a; Deng et al., 2018).

4. Results

4.1. Spatial variation in zircon Hf and crustal Hf model age

The Hf data are plotted in contour maps to show the spatial distribution of the controlling crustal features. The contour maps display a similar relationship between the zircon $\varepsilon_{Hf}(t)$ value and $T_{DM}c$

Table 1
Late Paleozoic tectonic framework.

Serial No.	Name of Sub-belt	Extent of Sub-Belt	Existing Knowledge on Tectonic Setting			References
			Metamorphic basement	Sedimentary covers	Magmatic groups	
1	NEKB	Bounded to the north to the NGF and to the south by the NKLF.	Paleoproterozoic Jinshuikou Group intermediate to high-grade metamorphic gneiss and amphibolite.	1. Ordovician–Silurian Qimantagh Group *meta*-clastic rocks. 2. Carboniferous-Lower Permian terrestrial clastic and carbonate rocks.	1. Granites, granodiorite and minor mafic rocks (ca. 469–360 Ma). 2. Monzogranite, diorite and granodiorite (ca. 240–200 Ma).	Yu et al., 2020; Zhong et al., 2021
2	CEKB	Bounded to the north to the NKLF and to the south by the CKLF	Paleoproterozoic Jinshuikou Group intermediate to high-grade metamorphic schist, gneiss, amphibolite, granulite, and minor limestone and migmatite.	1. The Devonian Maoniushan Formation terrestrial sandstone and conglomerate. 2. Carboniferous to Permian marine limestone and clastic sedimentary rocks. 3. The Triassic Elashan Formation intermediate-acidic calc-alkaline high-potassium terrestrial volcanic rocks.	1. Neoproterozoic S-type gneissic granites (ca. 1006–870 Ma). 2. Early Paleozoic diorites, granites and granodiorite (ca. 466–390 Ma). 3. Late Paleozoic to Mesozoic granites, diorites and mafic rocks (ca. 266–200 Ma).	He et al., 2016; Huang et al., 2014;Xia et al., 2014; Xiong et al., 2016
3	SEKB	Bounded to the north to the CKLF and to the south by the Bayan Har terrane	1. Paleoproterozoic high-grade metamorphic Kuhai group paragneiss, amphibolite, and limestone. 2. Meso-Neo Proterozoic intermediate metamorphic Wanbaogou group clastic and volcanic rocks.	1. Ordovician–Silurian low-grade metamorphism Naij Tal Group volcanic-sedimentary rocks. 2. Carboniferous-Lower Triassic volcanic and clastic rocks. 3. Middle Triassic turbidite and Upper Triassic molasse sequence.	1. Early Paleozoic intrusions are principally diorite, granodiorite, and granite (ca. 555–420 Ma). 2. Late Paleozoic to Mesozoic diorite, granodiorite, and granite (ca. 270–220 Ma).	Chen et al., 2012; Fan et al., 2022; Li et al., 2018b

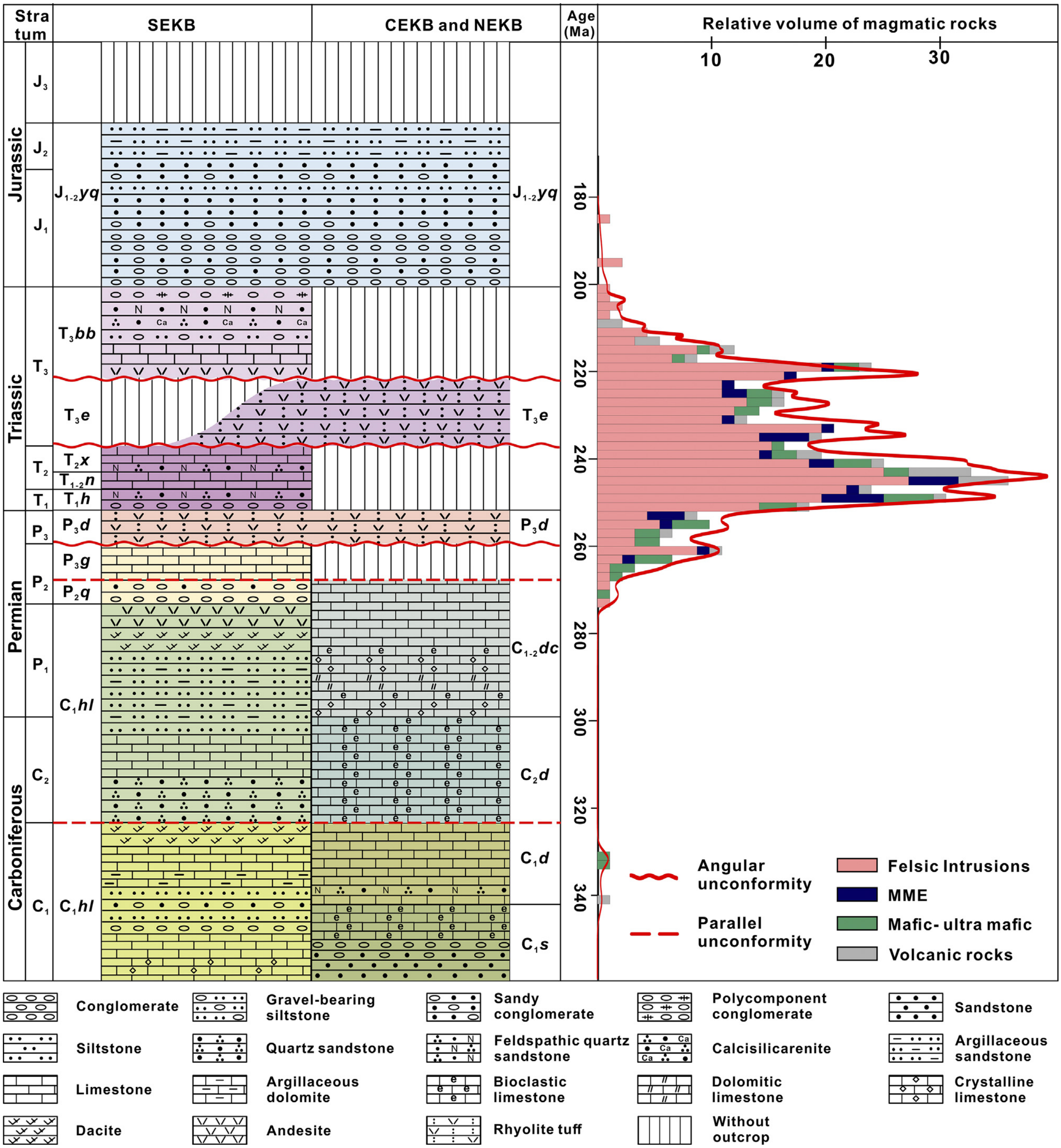

Fig. 3. The lithostratigraphic section of the Carboniferous-Jurassic strata and histogram of ages of Late Paleozoic–Mesozoic magmatism in the EKOB (The times of the unconformity are from Li et al., 2012; Chen et al., 2017). A summary of the zircon U-Pb results is listed in Supplementary Data Table S1.

(Fig. 5a, b). Domains in the NEKB (Wutumeiren area) show $\varepsilon_{Hf}(t)$ in the range of −6.4 to 12.5 (mean −0.4) and $T_{DM}c$ = 457–1661 Ma (mean 1285 Ma) (Supplementary Data Table S2). A low $\varepsilon_{Hf}(t)$ (< −2.4) with high $T_{DM}c$ (>1.3 Ga) and high $\varepsilon_{Hf}(t)$ (> −0.5) with low $T_{DM}c$ (<1.2 Ga) transition zone spatially corresponding to the CEKB (Fig. 5a, b). Domains in the SEKB show $\varepsilon_{Hf}(t)$ values in the range of −20.4 to 4.6 with a mean value of 2.5 and $T_{DM}c$ = 981 to 2524 Ma with a mean of ca. 1416 Ma. There are two negative $\varepsilon_{Hf}(t)$ domains around NaijTal ($\varepsilon_{Hf}(t)$ = −20.4 to −0.1, and $T_{DM}c$ = 1248 to 2524 Ma) and Gouli ($\varepsilon_{Hf}(t)$ = −11.6 to 0.9 and $T_{DM}c$ = 1438 to 1821 Ma) (Fig. 5a, b, Supplementary Data Table S2).

4.2. Crustal thickness of Late Paleozoic to Mesozoic in EKOB

The crustal thickness calculated by using the whole rock Sr/Y ratio displays a comparable relationship between whole rock $(La/Yb)_N$ ratios (Fig. 6a, b). Thus, the calculation of the crustal thickness supports the validity of the estimated moho depth. Domains in the NEKB show low Sr/Y and $(La/Yb)_N$ values in the range of 29.3–37.8 km and 13.9–30.3 km, respectively. Locally, there are high crustal thickness domains around Wutumieren (Sr/Y = 42.1–53.8 km, $(La/Yb)_N$ = 35.8–43.2 km, Fig. 6a, b). The CEKB is characterized by a thick and thin crust transition zone from west to east. Three thin

Table 2
Spatio-temporal distribution of ore forming system.

No.	Deposit	Type	Commodity	Size	Location	Formation/Group	Host rock	Rock age (Ma)	Ore forming age (Ma)	Data source
1	Yazigou	Skarn	Fe-Cu-Zn-Pb	Large	NEKB	Tianjianshan F.	Monzonite granite	U-Pb: 224 ± 4	Re-Os: 224.7 ± 3.4	Mi, 2019
2	Jingren		Fe-Pb-Zn	Large	NEKB	Tianjianshan F.	Granodiorite	U-Pb: 219.2 ± 1.4	Re-Os: 225 ± 4	Feng et al., 2011b
						Diaowusu F.			Re-Os: 229.9 ± 1.5	Dai, 2018
3	Hutouya		Fe-Pb-Zn	Large	NEKB	Langyashan F.	Granodiorite monzonitic	U-Pb: 227.1 ± 3.6	Re-Os: 225.0 ± 4.0	Gao et al., 2020
							Granite	U-Pb: 222.10 ± 0.98	Re-Os: 230.1 ± 4.7	Feng et al., 2011a
							Granite porphyry	U-Pb: 222.7 ± 2.5	Re-Os: 227.5 ± 5.5	Shi et al., 2017
4	Kendekeke		Fe-Au	Medium	NEKB	Tianjianshan F.	Adamellite	U-Pb: 229.5 ± 0.5	Sericite Ar-Ar: 222.4 ± 2.5	Xiao et al., 2013
5	Yemaquan		Fe	Large	NEKB	Tianjianshan F.	Monzonite granite	U-Pb: 229.5 ± 2.2		Liu et al., 2017b
6	Niukutou		Fe-Pb-Zn	Large	NEKB	Tianjianshan F.	Granite	U-Pb: 216.5 ± 3.3		Wang et al., 2021
								U-Pb: 212 ± 7.4		
7	Galinge		Fe	Large	NEKB	Tanjianshan G	Monzodiorite	U-Pb: 228 ± 2	Sericite Ar-Ar: 235.8 ± 1.7	Yu et al., 2017
							Adamellite	U-Pb: 228.0 ± 0.5		Gao et al., 2012
							Pyroxene diorite	U-Pb: 234.4 ± 0.6		Bai et al., 2016
10	Tawenchahan		Cu-Pb-Zn	Medium	NEKB	Tianjianshan F.	Granodiorite-porphyry	U-Pb: 236.0 ± 2.3	Ar-Ar: 229.9 ± 3.5	Yang, 2015
12	Kaerqueka		Cu–Pb–Zn	Large	CEKB	Tanjianshan G.	Porphyritic monzogranite	U-Pb: 227 ± 2	Re-Os: 246.1 ± 1.2	Gao et al., 2018
									Ar-Ar: 233.9 ± 1.4	
13	Suolajier		Cu-Mo	Small	CEKB	Tianjianshan F.	Biotite granodiorite		Re-Os: 238.8 ± 1.8	Feng et al., 2009
15	Balugou		Fe-Pb-Zn	Small	CEKB	Jinshuikou G.	Granite	U-Pb: 244.0 ± 1.9		Zhang, 2013
26	Xiaowolong		Fe-Cu-Sn	Medium	CEKB	Jinshuikou G.	Monzonite granite	U-Pb: 259.6 ± 1.8	Cassiterite U-Pb: 257.5 ± 4.3	Guo et al., 2020
29	Shenduolong		Fe-Au-Zn	Medium	CEKB	Jinshuikou G.	Diorite	U-Pb: 236.4 ± 1.6	Re-Os: 236.2 ± 2.1	Li et al., 2015a
33	Rilonggou		Cu-Sn	Large	SEKB	Elashan F.	Granodiorite	U-Pb: 230.7 ± 1.5		Wu et al., 2015
34	Saishentang		Cu-Mo	Large	SEKB	Elashan F.	quartz diorite	U-Pb: 222.6 ± 2.4	Re-Os: 223.4 ± 1.5	Wang et al., 2016b
14	Yanjingou	Vein type	Au	Large	CEKB	Jinshuikou G.	Granite	U-Pb: 260.4 ± 2.3	Rb-Rr: 237 ± 3	Chen et al., 2019
16	Shuizhadonggou		Au	Large	CEKB	Jinshuikou G.	Dioritic porphyrite	U-Pb: 220.3 ± 1.3	Sericite Ar-Ar: 230.8 ± 1.7	Feng, 2002
17	Huanglougou		Au	Large	CEKB	Jinshuikou G.	Granodiorite	U-Pb: 244.1 ± 2.0	Sericite Ar-Ar: 237 ± 2	Zhang et al., 2017
19	Balong		Au	Small	CEKB		Granodiorite	U-Pb: 229 ± 10	Pyrite Rb-Sr: 229.4	Huang et al., 2021
20	Naomuhunhe		Au	Medium	CEKB		Granodiorite	U-Pb: 235.8 ± 0.8	Sericite Ar-Ar: 228.86	Li, 2017
21	Asiha		Au	Medium	CEKB		Quartz diorite	U-Pb: 238.4	Sericite Ar-Ar: 202.6 ± 4.4	Li, 2017
							Granite porphyry	U-Pb: 234.9 ± 1.3	Monazite U-Pb: 227 ± 7	Liang et al., 2021
							Granodiorite	U-Pb: 222.1 ± 3.9	Sericite Ar-Ar: 234.63 ± 1.20	Chen et al., 2020
9	Changshan	Porphyry type	Mo	Small	CEKB	Jinshuikou G.	Granite	U-Pb: 220 ± 1	Re-Os: 218	Feng et al., 2010
11	Lalingzaohuo		Mo	Small	NEKB	Jinshuikou G.	Granodiorite	U-Pb: 242.6 ± 3.4	Re-Os: 214.5 ± 4.9	Wang et al., 2013
18	Qingshuihedong		Mo	Medium	CEKB	Jinshuikou G.	Granite	U-Pb: 222.7 ± 2.5	Sericite Ar-Ar: 214.5 ± 4.9	Wang et al., 2017b
23	Halongxiuma		Mo	Large	CEKB	Jinshuikou G.	Granodiorite-porphyry	U-Pb: 224.68 ± 0.88	Re-Os: 223.51 ± 1.30	Lu et al., 2017
24	Reshui		Mo	Large	CEKB	Jinshuikou G.	Monzonite	U-Pb: 230.9 ± 1.4	Re-Os: 230.2 ± 2.5	Zhu et al., 2018b
27	Duolongqiarou		Mo	Large	CEKB	Jinshuikou G.	Monzonite granite	U-Pb: 236.8 ± 1.8	Re-Os: 235.9 ± 1.4	Guo et al., 2022
28	Jiadanggen		Mo	Medium	CEKB	Elashan F.	Granodiorite-porphyry	U-Pb: 227 ± 1		Xu, 2014
31	Xiadeboli		Cu-Mo	Medium	SEKB	Hongshuichuan F.	Granite porphyry	U-Pb: 244.2 ± 2.1		Liu et al., 2012
32	Eikengdelesite		Cu-Mo	Medium	SEKB	Hongshuichuan F.	Monzonite granite	U-Pb: 248.4 ± 0.8		Xu, 2014
8	Mohexiala	Epithermal type	Ag-Pb-Zn	Medium	NEKB	Jinshuikou G.	Granite porphyry	U-Pb: 222 ± 1		Xu, 2014
22	Harizha		Ag-Pb-Zn	Large	CEKB	Jinshuikou G.	Granodiorite-porphyry	U-Pb: 233.6 ± 4.3		Duan, 2014
25	Nagengqieer		Ag-Pb-Zn	Large	CEKB	Elashan F.	Rhyolitic porphyry	U-Pb: 217.4 ± 3.1	Zircon U-Pb: 215.3 ± 3.1	Guo et al., 2019
30	Suolagou		Ag-Pb-Zn	Large	CEKB	Elashan F.	Syenogranite	U-Pb: 233 ± 1		Zhou, 2019

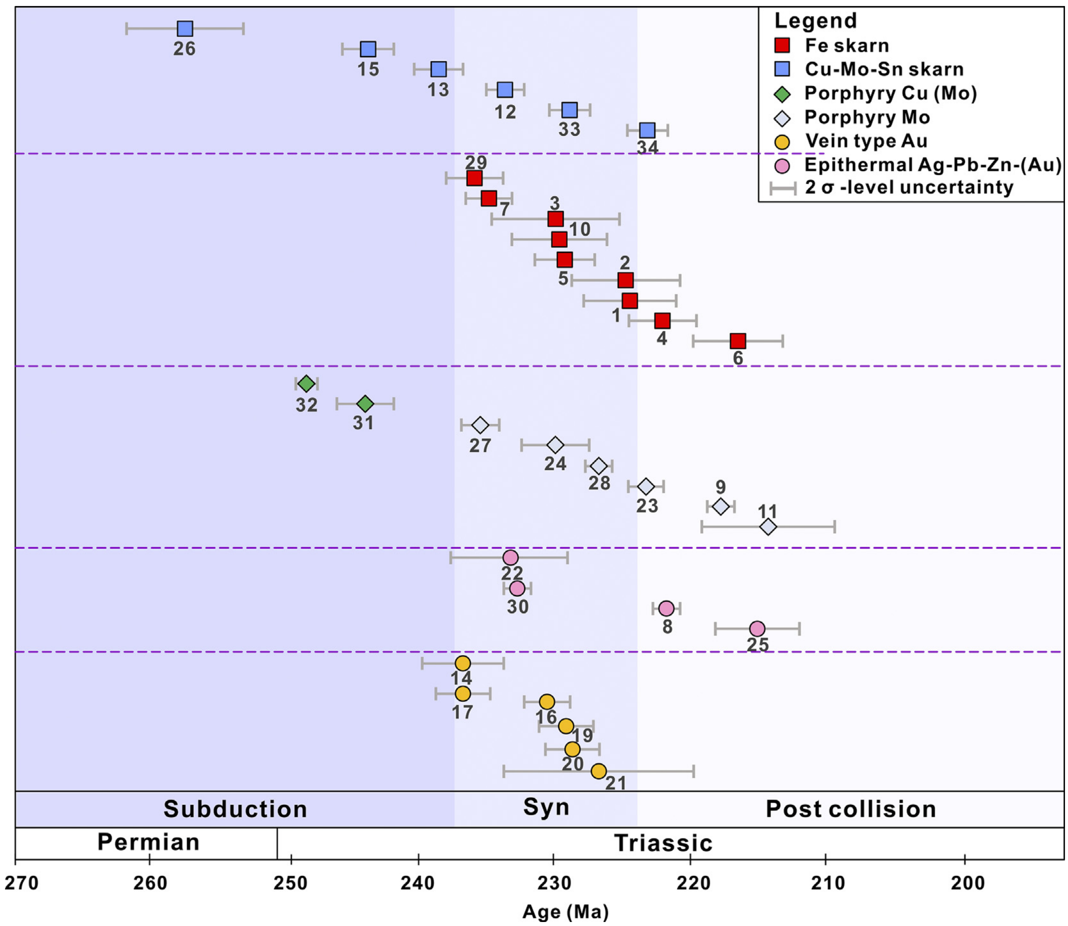

Fig. 4. Summary of the ore-forming age of significant ore deposits in the Eastern Kunlun orogenic belt. Geologic features of significant ore deposits labeled with numbers are listed in Table 2.

crustal thickness areas can be determined in Kaerqueka (Sr/Y = 38.5–40.9 km, $(La/Yb)_N$ = 26.2–35.8 km), Xiarihamu (Sr/Y = 37.8–40.9 km, $(La/Yb)_N$ = 26.2–35.8 km), Zongjia (Sr/Y = 37.8–40.9 km, $(La/Yb)_N$ = 20.8–30.3 km). In addition, two distinct areas are located in the Wulonggou (Sr/Y = 42.1–48.9 km, $(La/Yb)_N$ = 35.8–47.4 km) and Gouli areas (Sr/Y = 42.1–64.4 km, $(La/Yb)_N$ = 43.2–68.6 km) with the characteristics of thick crustal thickness. Domains in the SEKB show greater crustal thickness (Sr/Y = 42.1–51.0 km, $(La/Yb)_N$ = 40.1–68.6 km) but the crustal thickness is locally relatively thin in the NaijTal area (Sr/Y = 35.4–40.3 km, $(La/Yb)_N$ = 26.2–30.3 km).

5. Discussion

5.1. Implications for the evolution of the Paleo-Tethys Ocean

Based on the zircon U-Pb dataset (Supplementary Data Table S1), a three-stage magmatic emplacement sequence can be distinguished (Fig. 3). The first stage occurred during 270–240 Ma and was marked by numerous intrusions and volcanic rocks with arc-like affinities and the age of magmatism decreased from south to north, which is consistent with the geochemical polarity of northward subduction (Figs. 7 and 8, Thomas and Billen, 2009; Li et al., 2015b). Following this stage, the magmatism became diminished during ca. 240–237 Ma (Fig. 3). This gap matches well with the early compressional stage of the continental collision when magmatism is typically limited due to the increasing pressure (Xiong, 2014; Xia, 2017). Therefore, the Paleo-Tethys Ocean closure and initial accretionary collision processes are estimated to have occurred at about 240 Ma. Subsequently, the EKOB evolved to a post-collisional stage after ca. 224 Ma (Yao et al., 2017; Zhou et al., 2020). This is evidenced by the zircon $\varepsilon_{Hf}(t)$ values of the magmatic rocks which have been generated during the ca. 224–200 Ma phase exhibiting a gradually increasing trend and the crustal thickness decreased dramatically (Fig. 7b). Therefore, the tectonic evolution of the EKOB during the Late Permian to Late Triassic involved three stages: (1) subduction of the Paleo-Tethys Ocean during 270–240 Ma; (2) Middle Triassic continental collision (ca. 240–224 Ma); (3) a Late Triassic post-collisional (ca. 224–200 Ma) extensional setting. This conclusion is consistent with regional sedimentary and metamorphic events in this period, as summarized in Table 3.

5.2. Crustal architecture in different geodynamic settings

5.2.1. Oceanic subduction (270–240 Ma)

The granitoids in the subduction setting (ca. 270–240 Ma) are mainly medium–high K calc-alkaline series and enriched in large-ion lithophile elements (LILEs) and light rare-earth elements but depleted in high-field-strength elements (HFSEs) (Figs. 9, 10 and Supplementary Data Table S4). These rocks exhibit moderately

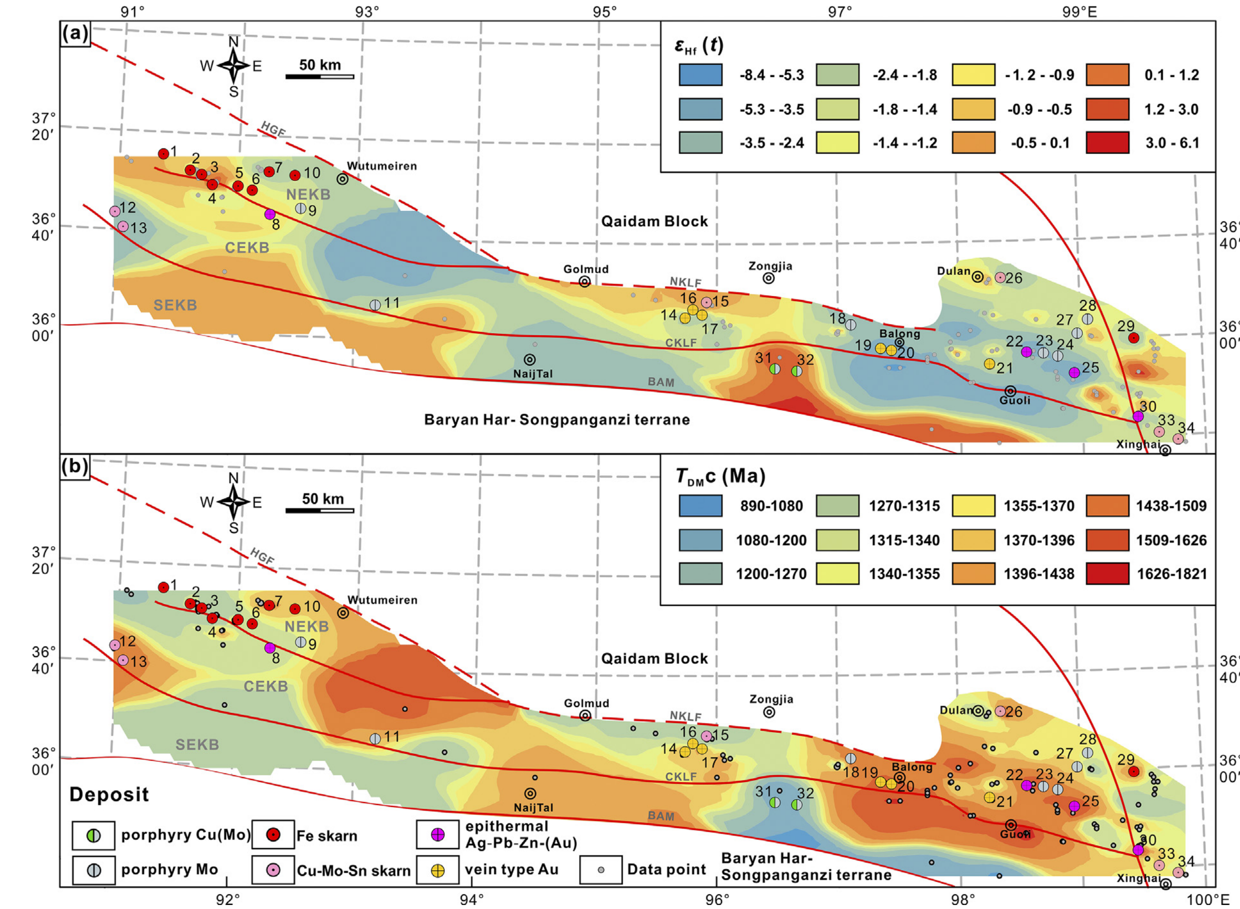

Fig. 5. (a) Isotope contour map showing the spatial variation of $\varepsilon_{Hf}(t)$ values and (b) zircon Hf crustal model ages, $T_{DM}C$ values, for the late Paleozoic–Mesozoic granitoid rocks and felsic volcanic rocks in the Eastern Kunlun orogenic Belt. Data are listed in Supplementary Data Table S3.

negative to positive $\varepsilon_{Hf}(t)$ values (−11.6 to +12.4) and two-stage Hf model ages ranging from 486 Ma to 2004 Ma (Fig. 7a, Supplementary Data Table S2). The occurrences of extensive MMEs and depleted Hf isotope values indicate that mantle material has contributed to the generation of these granitic rocks (Xiong et al., 2012; Chen et al., 2017). Additionally, slab melts have been suggested to account for contemporary regional magmatism with regards to the following aspects: (1) the subduction of an oceanic slab leads to fluid metasomatism, inducing partial melting of an enriched lithospheric mantle wedge (Zhao et al., 2019; Li et al., 2020); (2) mixing between the slab-derived and enriched mantle-derived melts also accounts for the regional granitoid rocks (Chen et al., 2017; Pan et al., 2022). Therefore, the growth of the bulk crust in the subduction setting is due to the contribution of both the slab and the subcontinental mantle to regional magmatism. As a result, the crust thickness slowly increased after ∼ 270 Ma, reaching ∼ 45 km at ∼ 240 Ma based on the $(La/Yb)_N$ and Sr/Y data (Fig. 7b).

5.2.2. Continental collision (240–224 Ma)

The magmatism generated during ca. 240–224 Ma exhibits a wider range of types and geochemical compositions compared to that generated in the subduction setting (ca. 270–240 Ma). This includes the development of extensive I-type granites, A-type granites, and intraplate-type mafic dykes (Ao et al., 2015; Zhang et al., 2016a; Liu et al., 2017a; Li et al., 2021). Moreover, granitoids generated in the *syn*-collision setting exhibit more pronounced negative Eu anomalies (Fig. 10c, d), variable zircon $\varepsilon_{Hf}(t)$ values (−24.6 to +10.5), and two-stage Hf model ages ranging from 597 Ma to 2810 Ma (Fig. 7a; Supplementary Data Table S2).

However, the recurrence of magmatic peaks and diverse compositions, particularly the occurrence of A-type granites and intraplate-type mafic dykes are typically generated in an extension setting (Whalen et al., 1987; King et al., 1997; Bonin, 2007). This suggests lithospheric extension in an overall compressional continental collision setting. In this study, the preferred interpretation is the oceanic slab break-off model. The model suggests that the hot asthenospheric mantle ascended through the slab window, not only creating a transient and thermal anomaly in the overlying lithospheric mantle but also causing both thermal erosion and mechanical deformation of the lower crust (Ratschbacher et al., 2003; Roy et al., 2014; Tesauro et al., 2018). This results in the generation of transient magmatic pulses with intraplate characteristics and leads to extensional deformation and localized thinning of the crust thickness. Consequently, the overall crustal thickness exhibit thickening, but local areas of thinning were also observed, with a wide range of 25–60 km (Fig. 7b). Additionally, there was a negative correlation between $\varepsilon_{Hf}(t)$ values and crust thickness both spatially and temporally (Figs. 5–7).

5.2.3. Post-collision extension (224–200 Ma)

The magmatic rocks generated during ca. 224–200 Ma shows high contents of SiO_2, Na_2O, and K_2O and are slightly peraluminous (A/CNK = 1.03–1.07; Figs. 9, 10e and f, Supplementary Data Table S4), exhibits variable zircon $\varepsilon_{Hf}(t)$ values (−20.2 to +12.5) and two-stage Hf model ages from 457 Ma to 2524 Ma (Fig. 7a; Supplementary Data Table S2), most of the $\varepsilon_{Hf}(t)$ values exhibit

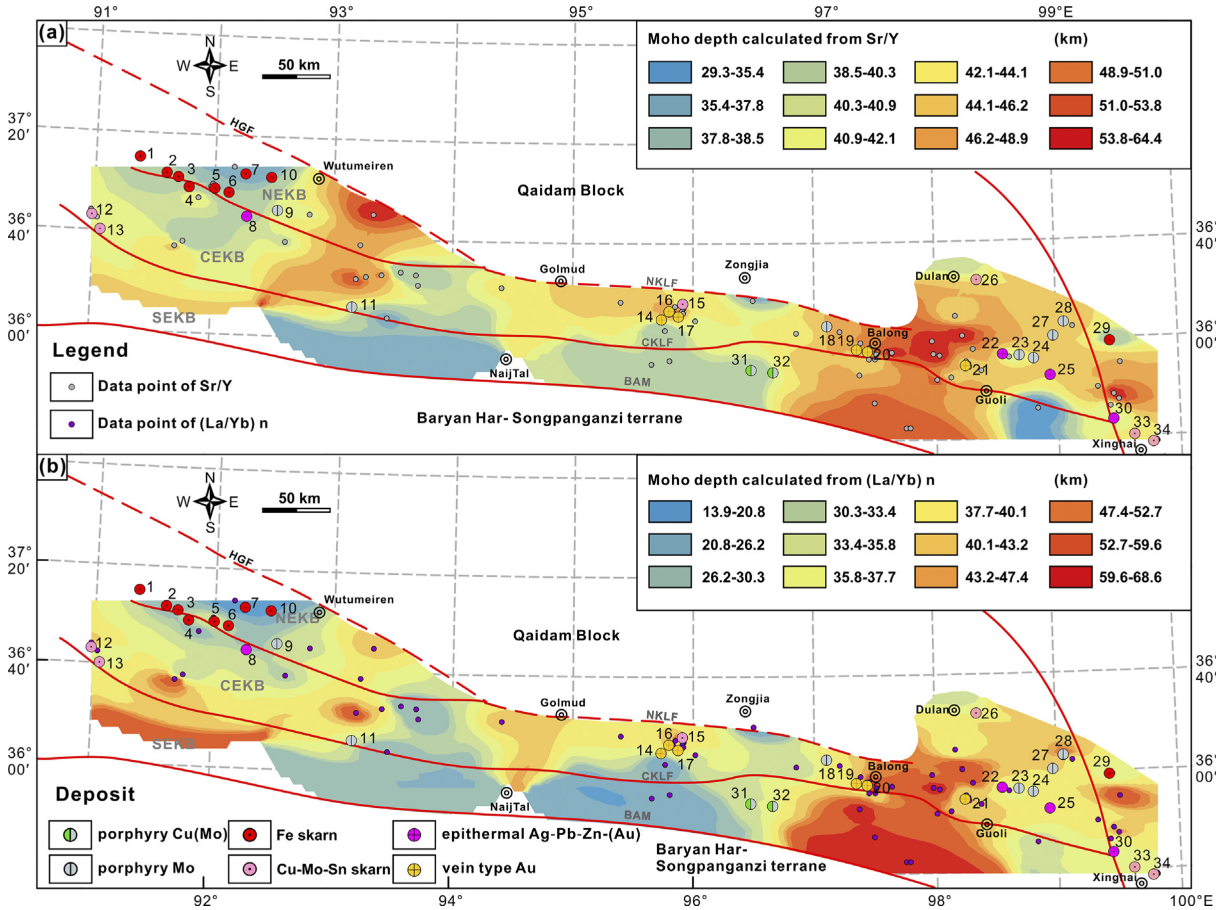

Fig. 6. (a) Crust thickness calculated by whole rock Sr/Y values and (b) whole rock $(La/Yb)_N$ values for the late Paleozoic–Mesozoic granitoid rocks and felsic volcanic rocks contour map showing the crust thickness spatial variation in Eastern Kunlun Orogenic Belt. The data are listed in Supplementary Data Table S7.

negative values and old T_{DM}c ages (Fig. 7a), indicating that ancient continental crust has played a significant role in their formation (Zhao et al., 2019; Zhao et al., 2020). Previous studies suggest that the thickened lower crust underwent delamination during ca. 224–200 Ma, evidenced by the presence of high-Mg adakite (Chen et al., 2013), alkaline granitoids, OIB-type mafic dykes, and high-Nb-Ta rhyolites in the EKOB (Hu et al., 2016; Liu et al., 2017a; Zhu et al., 2022). In comparison to slab break-off, delamination causes large-scale asthenospheric upwelling that can provide additional heat to melting of ancient crust and crustal thinning. As result, the thickness of the crust decreased dramatically and reached ~ 45 km at around 200 Ma (Fig. 7b).

5.3. Correlation between the lithospheric architecture and location of ore deposits

*5.3.1. Porphyry-type deposi**t***

The porphyry mineralization in the EKOB includes Late Permian to Early Triassic porphyry Cu-Mo deposits generated in relation to the subduction setting, and Middle to Late Triassic porphyry Mo deposits formed during continental collision and in post-collision extensional settings (Fig. 4).

The subduction-related porphyry Cu-Mo deposits occur in regions with high $\varepsilon_{Hf}(t)$ values, low Hf model T_{DM}c ages with medium crustal thickness (37.7–40.3 km; Fig. 11). Ore-related granitoids exhibit positive zircon $\varepsilon_{Hf}(t)$ values (+2.4 to +4.6), Hf model T_{DM}c ages of 981–1123 Ma, and enrichment in LREE, Rb, Ba, Th, U and K, but depletion in Nb, Ta, Sr, P and Ti, indicating their origin from the juvenile lower continental crust (Yang et al., 2018). This interpretation is consistent with previous studies from the Tibet Plateau, that the juvenile continental crust shows a delivered dominant contribution of material for the generation of porphyry Cu deposits (Hou et al., 2007; Hou et al., 2015). Furthermore, because of the northward subduction of the Paleo-Tethys Ocean in the EKOB, the juvenile components in magmas decreased gradually from south to north, due to increasing crustal input in the north, following subduction polarity. Therefore, porphyry Cu-Mo deposits are primarily associated with magmatic rocks formed during the early stages of subduction and are typically located in the southern region in the EKOB (Fig. 12).

The Middle to Late Triassic porphyry Mo mineralization occurs in regions with low $\varepsilon_{Hf}(t)$ values, high Hf model T_{DM}c ages and variable crustal thickness (30.3–51.0 km; Fig. 11). These magmatic rocks related to the Middle to Late Triassic porphyry Mo deposits

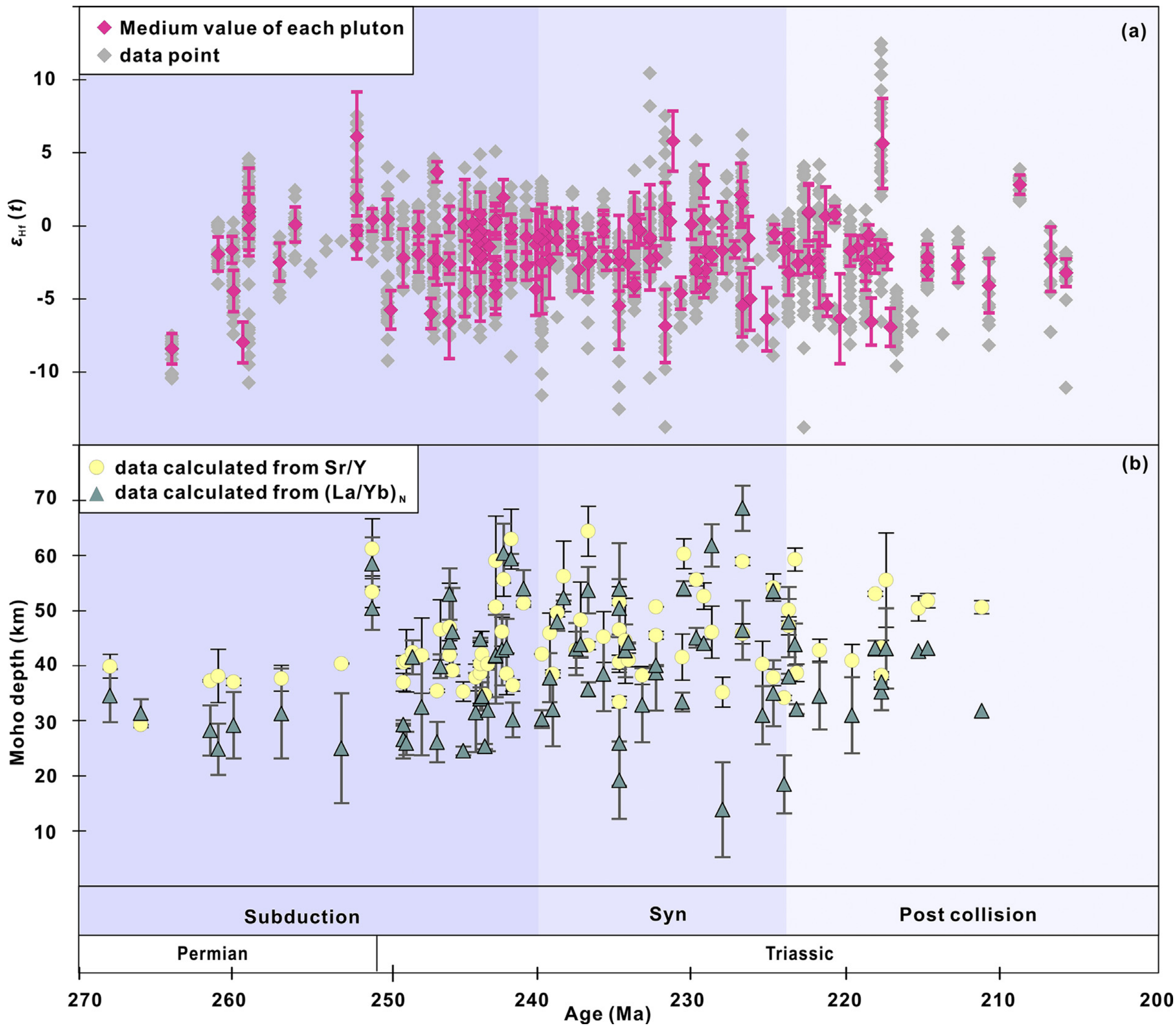

Fig. 7. (a) Age versus $\varepsilon_{Hf}(t)$ and (b) Age versus crust thickness of published late Paleozoic–Mesozoic granitoid rocks and felsic volcanic rocks. The data are presented in Supplementary Data Tables S2, S3, and S7 respectively.

are characterized by $\varepsilon_{Hf}(t)$ = −12.3 to −0.5, and T_{DM}c = 1297–2056 Ma (Guo, 2020; Han et al., 2020). These Hf enriched isotopic compositions of the magmatic rocks accounting for the Middle to Late Triassic porphyry Mo deposits indicate that more ancient crust materials contribution. The conclusion is supported by the studies of the Tibet Plateau and Qingling Orogenic Belt, in which the Mo-related intrusions originated from an ancient crust-dominated source with evolved isotopic compositions and old T_{DM}-c ages (Hou et al., 2015; Richards, 2015; Li et al., 2018a). Additionally, molybdenum mineralization occurring in the *syn*-collisional setting occurred in a crustal thickness of 37.7–44.1 km (Fig. 13), whereas in post-collisional settings the crustal thickness was around 26.2–37.8 km (Fig. 14). The difference is caused by different anatexis of crust melting. In the continental collision setting, anatexis is the key to the melting of the ancient continental crust due to the heat accumulation in the thickened crust, while in post-collision settings, it is caused by increased heat input through asthenospheric upwelling (Bea, 2012; Zhu et al., 2018a).

5.3.2. Skarn-type deposit

Iron skarn deposits can be generated in both syn- and post-collisional settings (Fig. 4). These deposits occurring in regions with high $\varepsilon_{Hf}(t)$ values ($\varepsilon_{Hf}(t)$ = −1.8 to +6.1), low model T_{DM}c ages (T_{DM}c = 1080–1370 Ma, Fig. 5a, b), and with a thin crust (20.3–38.5 km; Fig. 6a, b). The intrusions associated with these iron skarn deposits often exhibit depleted isotopic compositions and high MgO contents (2.06–3.80 wt.%), indicating a stronger contribution from asthenosphere-derived melt (Xiao et al., 2013). As discussed in Sections 5.2.2 and 5.2.3, the upwelling of asthenosphere events in the EKOB at ca. 237 Ma, caused by slab break-off and lithosphere delamination at ca. 224 Ma, can lead to local extension in *syn*-collision settings and regional extension in post-collision settings. As a result, the spatial distribution of iron skarn deposits is mainly associated with regions of crustal thinning (Figs. 13 and 14).

The Cu-Mo-Sn skarn deposit are formed in either subduction, syn collision, or post-collision settings (Fig. 4), and show similar

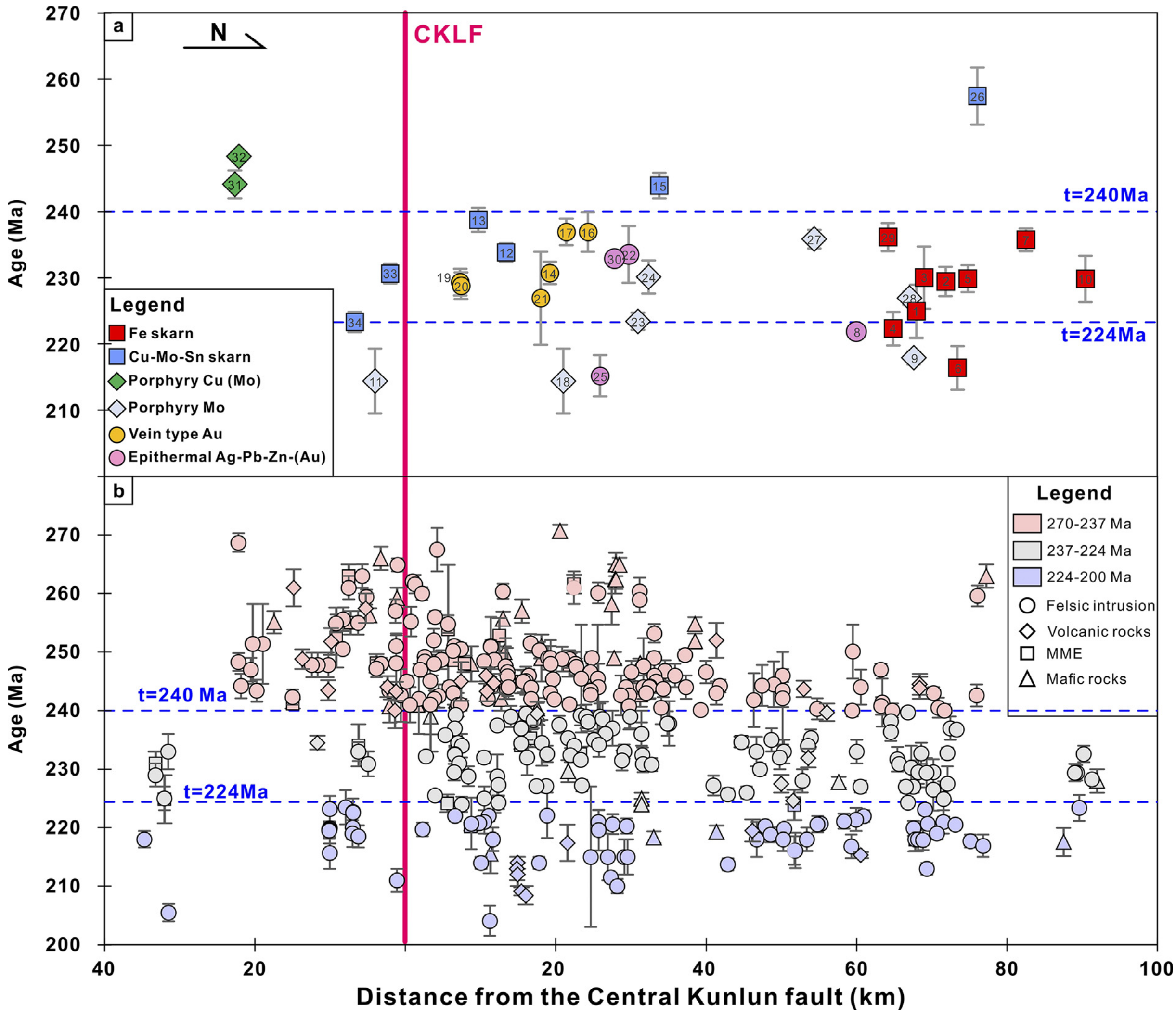

Fig. 8. (a) The mineralization age of deposits and (b) zircon U-Pb age variations with the distance to the Central Kunlun fault. The data are presented in Supplementary Data Tables S1 and Table 2 respectively.

Table 3
Summary of Late Paleozoic-Mesozoic magmatic-sedimentary-metamorphic features.

Evolution stage	Magma period (Ma)	Magma assemblage	Sedimentary and metamorphic features	Reference
Subduction	270–240	Diorite, granodiorite, and granite often contained abundant MME	1. The Late Permian Gequ Formation deposited during 260–252 Ma; consists of molasse sediments deposited in an oceanic environment; 2. The schist to amphibolite-facies metamorphic rocks in the Qingshuiquan district ca. 246–244 Ma.	Li et al., 2012; Xia et al., 2017
Syn-Collision	240–224	I-type granites, A-type granites, mafic dyke swarms, and adakite-like granitoids	1. The unconformable contact between the Early to Middle Triassic marine Xilikete Formation sediments and the Middle to Late Triassic lacustrine-facies Elshan Formation; 2. The Middle Triassic strata are absent in the SEKB; 3 The transformation from open to tight folding during the Middle Triassic.	Chen et al., 2017; Li et al., 2012;Qu et al., 2019
Post-Collision	224–200	Voluminous alkaline mafic dyke swarm, A-type granites, adakite-like granites, high Nb-Ta rhyolites, and bimodal volcanic rocks	1. The regional angular unconformity between the Middle Triassic Xilikete Formation and the Late Triassic Babaoshan Formation in the EKOB; 2. Analysis of the stress patterns in mafic dikes from the early and late Triassic periods shows a shift from a strike-slip stress regime to a tensile stress regime.	Hu et al., 2016; Xia et al., 2014; Xiong, 2014

Note: MME = Mafic microgranular enclaves.

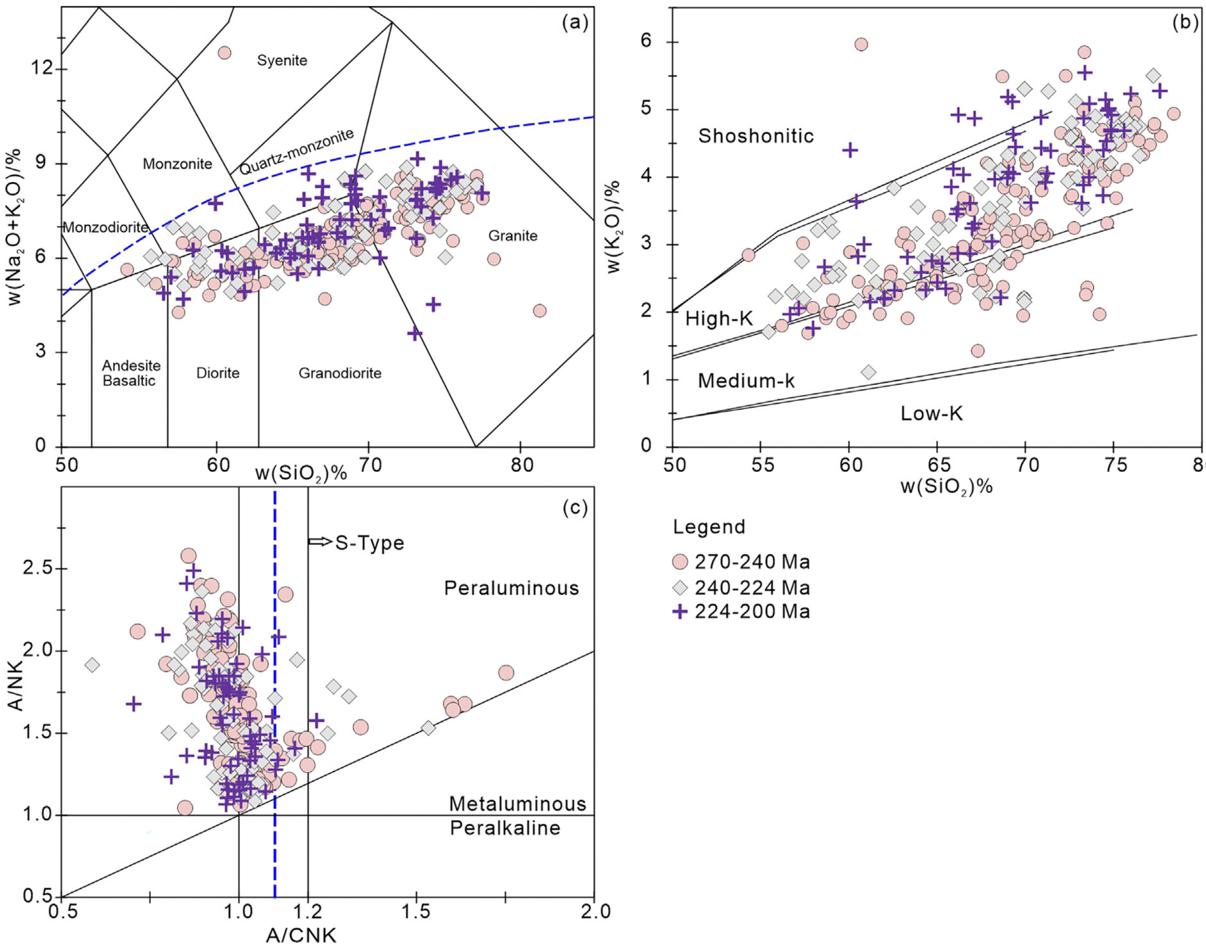

Fig. 9. (a) Plots of $Na_2O + K_2O$ versus SiO_2 contents (TAS) diagram (Le Bas et al., 1986). (b) SiO_2 versus K_2O diagram (Peccerillo and Taylor, 1976). (c). A/NK vs. A/CNK diagram, where A/NK is the molar ratio of $Al_2O_3/(Na_2O + K_2O)$ and A/CNK is the molar ratio of $Al_2O_3/(CaO + Na_2O + K_2O)$ (Maniar and Piccoli, 1989); The average data of the same rock type from the same pluton were used for plotting. Data are listed in Supplementary Data Table S4.

geochemical characteristics. These skarn deposits are located in a region with medium $\varepsilon_{Hf}(t)$ values, and $T_{DM}c$ ages ($\varepsilon_{Hf}(t)$ = −3.5 to −1.2, $T_{DM}c$ = 1355–1438 Ma, Fig. 5a, b), and increased crustal thickness (35.8–46.2 km; Fig. 6a, b).

Granitic intrusions related to Cu-Mo-Sn mineralization belong to high-K calc-alkaline and metaluminous to weakly peraluminous I-type granitoids (Gao et al., 2015; Fu et al., 2016; Wang et al., 2018; Guo et al., 2020). They display variable zircon $\varepsilon_{Hf}(t)$ values (Supplementary Data Table S2) and commonly contain MMEs (Gao et al., 2015; Wang et al., 2016b). These characteristics indicate that rocks related to Cu-Mo-Sn mineralization are derived from the partial melting of ancient lower continental crust with an additional input of mantle components (Liu et al., 2006; Feng et al., 2011a; Wang et al., 2016b). The mixing of continental crust and mantle rocks occurred during the entire orogeny in the EKOB. Consequently, the Cu-Mo-Sn skarn deposits formed during all stages of the orogeny.

5.3.3. Vein-type Au deposit

Vein-type Au deposits are mainly found in a *syn*-collisional setting that occurred between ca. 240–227 Ma. They are typically located in regions with low $\varepsilon_{Hf}(t)$ values ($\varepsilon_{Hf}(t)$ = −8.4 to −3.5), Mesoproterozoic Hf model $T_{DM}c$ ages ($T_{DM}c$ = 1355–1821 Ma; Fig. 5), and thick crustal thickness (40.1–48.9 km; Fig. 6). Thick crustal regions are more likely to undergo deformation and faulting, which can create the necessary structural conditions for the formation of vein-type gold deposits (Groves et al., 1998; Groves et al., 2005). Additionally, thick crustal areas may preserve gold-bearing fluids due to reduced permeability and increased likelihood of fluid entrapment (Bierlein et al., 2006). The Vein-type Au deposits in EKOB are spatially and temporally associated with Middle Triassic magmatism, which provided the ore-forming fluids and metals for Au mineralization (Liang et al., 2021; Wu et al., 2021b). Thus, the thick crustal regions, with their unique geological and tectonic features, provide a favorable environment for the formation of vein-type Au deposits during the collisional stage (Fig. 13).

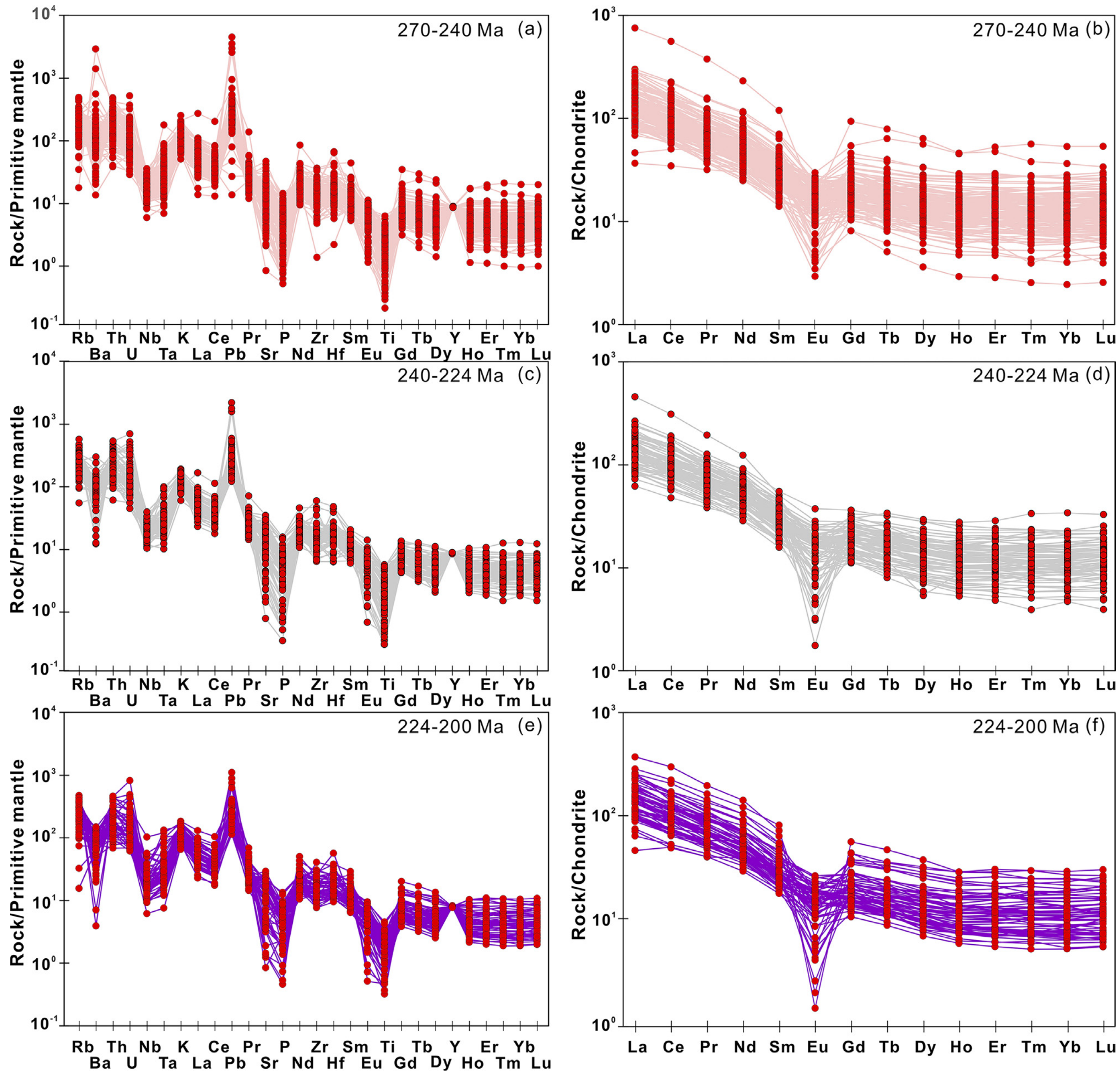

Fig. 10. REE and trace element patterns of the Late Paleozoic–Mesozoic granitoid rocks and felsic volcanic rocks in different evolution stages of the Eastern Kunlun Orogen (Chondrite and primitive-mantle values are from Sun et al., 1989). The average data of the same rock type from the same pluton were used for plotting. Data are listed in Supplementary Data Table S4.

5.3.4. Epithermal type Ag-Pb-Zn-(Au) deposit

The epithermal Ag-Pb-Zn-(Au) deposits in the EKOB are formed in both *syn*-collisional and post-collisional settings. Ore-related granites show low $\varepsilon_{Hf}(t)$ values ($\varepsilon_{Hf}(t)$ = −24.6 to −1.0) and old $T_{DM}c$ ages ($T_{DM}c$ = 1191–2810 Ma; Figs. 5 and 6). These isotopic characteristics suggest that the magmatism related to the epithermal Ag-Pb-Zn-(Au) deposits originated from the partial melting of ancient crust with an additional input of mantle components (Zhang et al., 2016b; Guo, 2020). However, the epithermal Ag-Pb-Zn-(Au) mineralization in the *syn*-collisional setting is located in the thicker portion of the continental crust (37.7–46.2 km). In contrast, in the post-collisional setting such epithermal Ag-Pb-Zn-(Au) deposits are located in an area of thinner crustal thickness (26.2–38.5 km). The similar isotopic characteristics but the different crustal thickness of epithermal Ag-Pb-Zn-(Au) mineralization in the syn- and post-collision settings were probably resulted from the different melting mechanisms of ancient crust, similar to magmatic rocks for the Middle to Late Triassic porphyry Mo mineralization.

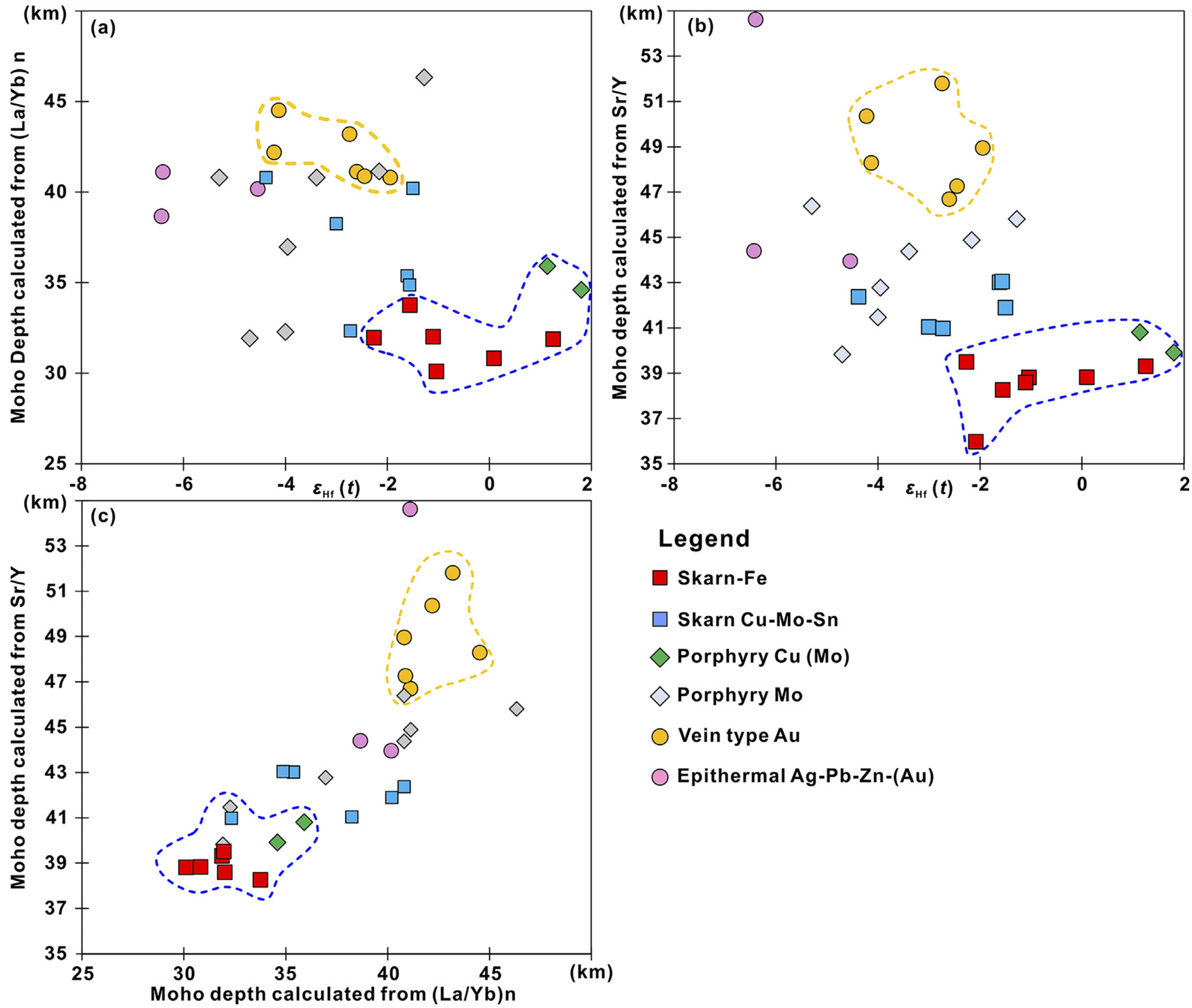

Fig. 11. (a) The zircon $\varepsilon_{Hf}(t)$ variation with crust thickness was calculated by $(La/Yb)_N$. (b) The zircon $\varepsilon_{Hf}(t)$ variation with crust thickness calculated by Sr/Y, (c) variation of $(La/Yb)_N$, and Sr/Y using calculated crustal thickness for the EKOB deposit are extracted from Figs. 7a, 8a and 8b, respectively.

6. Conclusions

Combined with the zircon Hf isotopic mapping and the evaluated crustal thickness, our study provides new insights into the metallogeny in the EKOB with the following major conclusions.

(1) The Fe skarn and porphyry Cu-Mo deposits in EKOB occur in the Moho uplift region characterized by relatively thin crust. Magmatism associated with porphyry Cu-(Mo) and Fe polymetallic skarn mineralization with high $\varepsilon_{Hf}(t)$ and $T_{DM}c$ values mainly originated from a juvenile crustal source.
(2) The magmatism associated with porphyry Mo and epithermal Ag-Pb-Zn-(Au) mineralization in the EKOB with low $\varepsilon_{Hf}(t)$ and high $T_{DM}c$ values originated mainly from the reworked ancient continental crustal material with a limited contribution from a mantle source.
(3) The main occurrence of vein-type Au is in the area of a depression of the Moho surface. Gold mineralization-related magmatism with low $\varepsilon_{Hf}(t)$ and high $T_{DM}c$ values indicate the involvement of older reworked crustal sources.
(4) The links between mineral deposits and Hf isotopic composition established in our study promise scope for exploration of mineral deposits at greater depths, particularly in large magmatic-hydrothermal domains.

CRediT authorship contribution statement

Xinming Zhang: Conceptualization, Data curation, Writing – original draft, Funding acquisition. **Xu Zhao:** Conceptualization, Funding acquisition, Supervision. **Lebing Fu:** Conceptualization, Methodology. **Yanjun Li:** Methodology, Funding acquisition. **Andreas Kamradt:** Writing – review & editing. **M. Santosh:** Writing – review & editing. **Chongwen Xu:** Data curation. **Xiaokun Huang:** Data curation, Visualization. **Gregor Borg:** Writing – review & editing. **Junhao Wei:** Project administration, Funding acquisition.

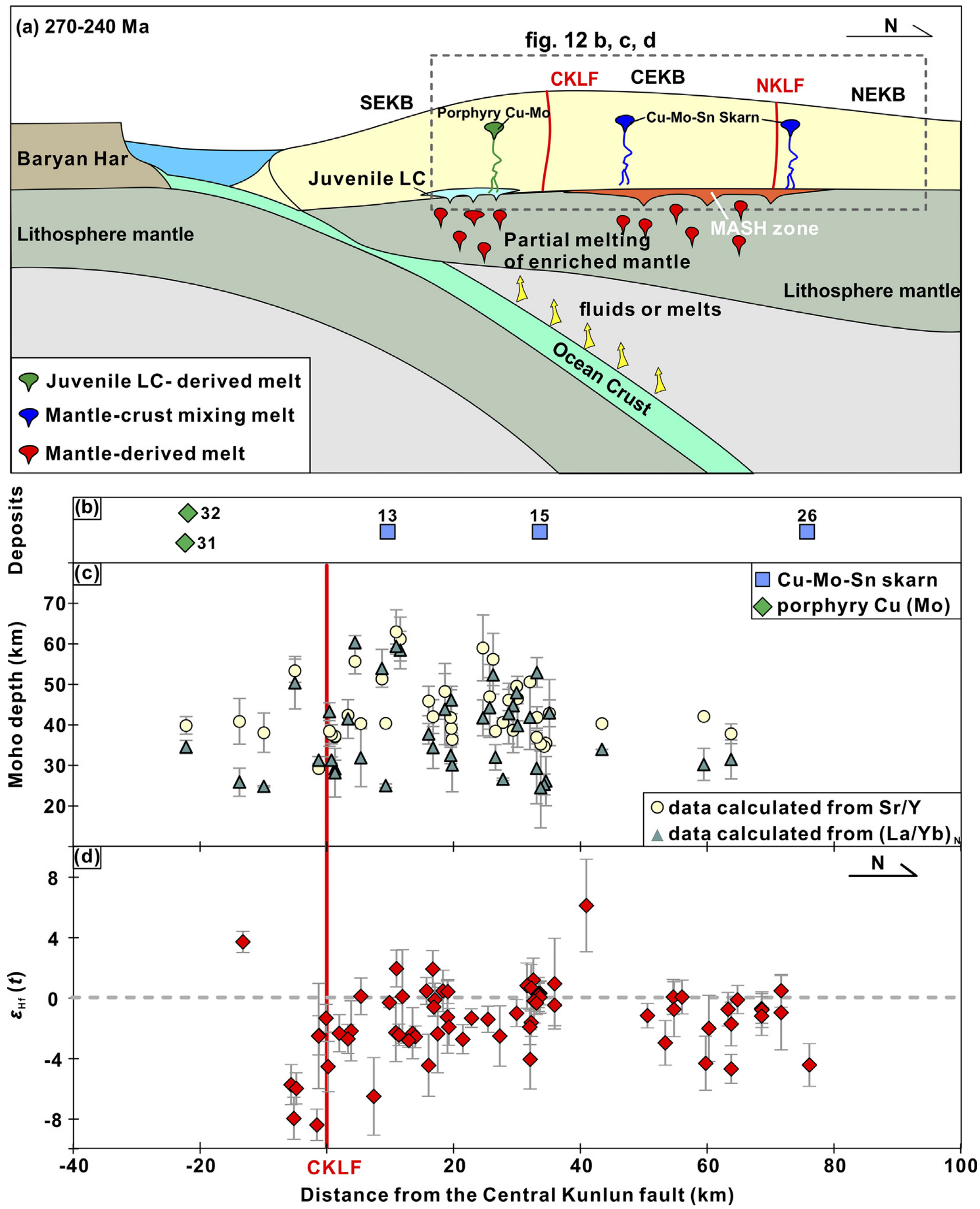

Fig. 12. (a) The late Permian magmatism was triggered by northward subduction ca. 270–240 Ma of the Paleo-Tethys oceanic (Xiong et al., 2019; Guo et al., 2020). (b) Variation of deposits, (c) zircon $\varepsilon_{Hf}(t)$ for granitic, felsic volcanic rocks and (d) crustal thickness during ca. 270–240 Ma with distance from the Central Kunlun Fault. The data are presented in Supplementary Data Tables S2, S3, and S7 respectively.

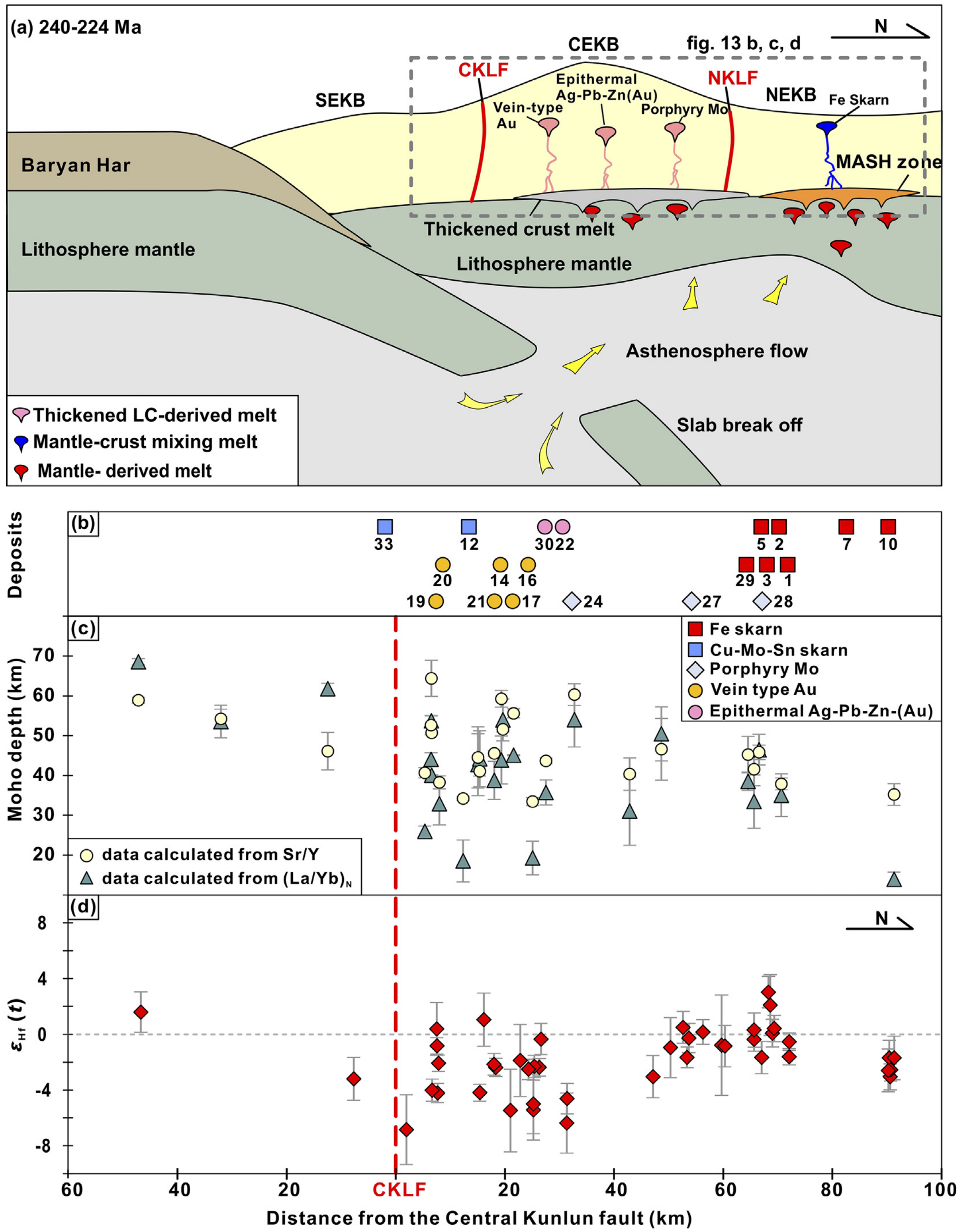

Fig. 13. (a) The early Triassic magmatism was triggered by slab break-off of the subducted Paleo-Tethys oceanic slab during the collision (Dai et al., 2013; Xue et al., 2020). (b) Variation of deposits, (c) zircon $\varepsilon_{Hf}(t)$ for granitic and (d) felsic volcanic rocks and crustal thickness during c. 240–224 Ma with distance from the Central Kunlun Fault. The data are presented in Supplementary Data Tables S2, S3, and S7 respectively.

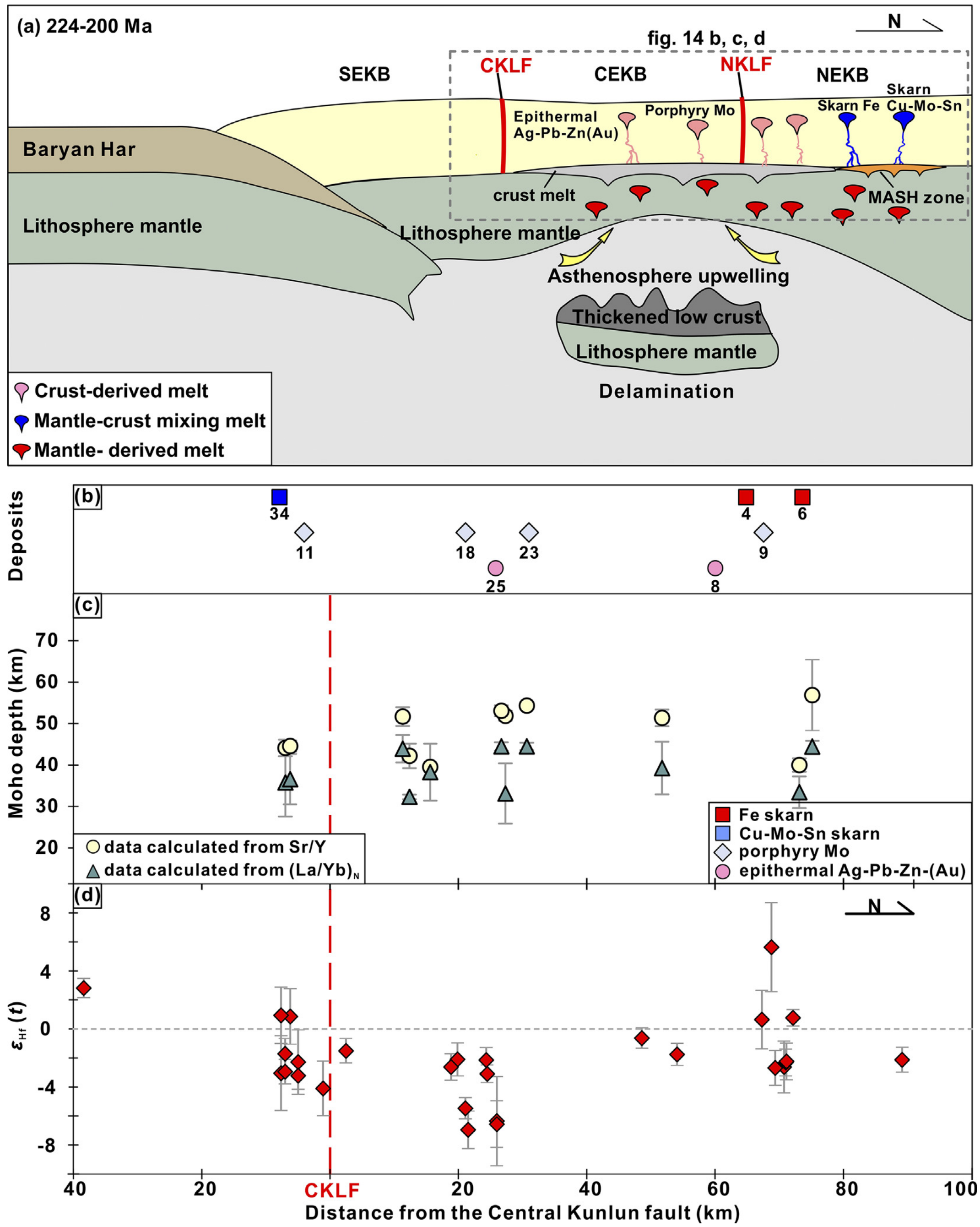

Fig. 14. (a) Later Triassic magmatism was triggered by delamination, which resulted in large-scale upwelling of the asthenospheric mantle and led to the whole-scale melting of the lower crust and the metasomatized subcontinental lithospheric mantle (ca. 224–200 Ma) (Peng et al., 2017; Zhou et al., 2020). (b) Variation of deposits, (c) zircon $\varepsilon_{Hf}(t)$ for granitic and felsic volcanic rocks and (d) crustal thickness during c. 224–200 Ma with distance from the Central Kunlun Fault. The data are presented in Supplementary Data Tables S2, S3, and S7 respectively.

Declaration of Competing Interest

The authors declare that they have no known competing financial interests or personal relationships that could have appeared to influence the work reported in this paper.

Acknowledgments

This study was financed by the National Natural Science Foundation of China (No. 42172084), China Postdoctoral Science Foundation (2021M693191), Geological Exploration Fund of the Qinghai Provincial, China (No. 2021074001ky001), and China Scholarship Council (CSC). Thanks to Associate Editor Prof. C. Manikyamba and the two anonymous reviewers for their insightful comments and suggestions, which helped to improve the quality of the paper. Special thanks to Zhixin Zhao, Shengtao Zhang, Weiwei Li, Xiaolong Li, and Bin Li from China University of Geosciences (Wuhan) for their assistance in data collection, as well as Jinmeng Li from the Chinese University of Hong Kong for her help in improving the language.

Appendix A. Supplementary data

Supplementary data to this article can be found online at https://doi.org/10.1016/j.gsf.2023.101654.

References

Ao, Z., Sun, F.Y., Li, B.L., Wang, G., Li, L., Li, S.J., Zhao, J.W., 2015. U-Pb Dating, geochemistry and tectonic implications of Xiaojianshan gabbro in Qimantage Mountain, Eastern Kunlun Orogenic Belt. Geotecton. Metallog. 39 (6), 1176–1184 (in Chinese with English abstract).

Bai, Y.N., Sun, F.Y., Qian, Y., Liu, H.C., Zhang, D.M., 2016. Zircon U-Pb geochronology and geochemistry of pyroxene diorite in Galinge iron-polymetallic deposit, East Kunlun. Glob. Geol. 35 (01), 17–27 (in Chinese with English abstract).

Bea, F., 2012. The sources of energy for crustal melting and the geochemistry of heat-producing elements. Lithos 153, 278–291. https://doi.org/10.1016/j.lithos.2012.01.017.

Bierlein, F.P., Gray, D.R., Foster, D.A., 2002. Metallogenic relationships to tectonic evolution – the Lachlan Orogen, Australia. Earth Planet. Sci. Lett. 202 (1), 1–13. https://doi.org/10.1016/S0012-821X(02)00757-4.

Bierlein, F.P., Groves, D.I., Goldfarb, R.J., Dubé, B., 2006. Lithospheric controls on the formation of provinces hosting giant orogenic gold deposits. Mineral. Deposita 40 (8), 874–886. https://doi.org/10.1007/s00126-005-0046-2.

Bonin, B., 2007. A-type granites and related rocks: evolution of a concept, problems and prospects. Lithos 97 (1–2), 1–29. https://doi.org/10.1016/j.lithos.2006.12.007.

Bouilhol, P., Jagoutz, O., Hanchar, J.M., Dudas, F.O., 2013. Dating the India-Eurasia collision through arc magmatic records. Earth Planet. Sci. Lett. 366, 163–175. https://doi.org/10.1016/j.epsl.2013.01.023.

Chen, Y.J., 2013. The development of continental collision metallogeny and its application. Acta Petrol. Sin. 29 (01), 1–17 (in Chinese with English abstract).

Chen, G.C., Pei, X.Z., Li, R.B., Li, Z.C., Pei, L., Liu, Z.Q., Chen, Y.X., Liu, C.J., 2013. Zircon U-Pb geochronology, geochemical characteristics and geological significance of Cocoe A'Long quartz diorites body from the Hongshuichuan area in East Kunlun. Acta Geol. Sin. 87 (2), 178–196 (in Chinese with English abstract).

Chen, B.L., Wang, Y., Han, Y., Chen, J.L., 2019. Metallogenic age of Yanjingou gold deposit in Wulonggou gold orefield, Eastern Kunlun Mountains. Miner. Deposits 38 (03), 541–556 (in Chinese with English abstract).

Chen, J.J., Wei, J.H., Fu, L.B., Li, H., Zhou, H.Z., Zhao, X., Zhan, X.F., Tan, J., 2017. Multiple sources of the Early Mesozoic Gouli batholith, Eastern Kunlun Orogenic Belt, Northern Tibetan Plateau: linking continental crustal growth with oceanic subduction. Lithos 292, 161–178. https://doi.org/10.1016/j.lithos.2017.09.006.

Chen, J.J., Fu, L.B., Selby, D., Wei, J.H., Zhao, X., Zhou, H.Z., 2020. Multiple episodes of gold mineralization in the East Kunlun Orogen, western Central Orogenic Belt, China: constraints from Re-Os sulfide geochronology 103587 Ore Geol. Rev. 123. https://doi.org/10.1016/j.oregeorev.2020.103587.

Chen, X.H., Gehrels, G., Yin, A., Li, L., Jiang, R.B., 2012. Paleozoic and Mesozoic Basement Magmatisms of Eastern Qaidam Basin, Northern Qinghai-Tibet Plateau: LA-ICP-MS zircon U-Pb geochronology and its geological significance. Acta Geol. Sin. (English Ed.) 86 (2), 350–369. https://doi.org/10.1111/j.1755-6724.2012.00665.x.

Dai, W., 2018. Ore-forming geological characteristic and prospecting potential for Pb-Zn polymetallic deposit in Jingren region of Qimantage area, Qinghai Province. Master Thesis, Jilin University, p. 67 (in Chinese with English abstract).

Dai, J.G., Wang, C.S., Hourigan, J., Santosh, M., 2013. Multi-stage tectono-magmatic events of the Eastern Kunlun Range, northern Tibet: insights from U-Pb geochronology and (U–Th)/He thermochronology. Tectonophysics 599, 97–106. https://doi.org/10.1016/j.tecto.2013.04.005.

Deng, J., Wang, Q.F., Li, G.J., 2017. Tectonic evolution, superimposed orogeny, and composite metallogenic system in China. Gondwana Res. 50, 216–266. https://doi.org/10.1016/j.gr.2017.02.005.

Deng, J., Wang, C.M., Leon, B.M., Enya, Y.S., 2018. Crustal architecture and metallogenesis in the south-eastern North China Craton. Earth-Sci. Rev. 182, 251–272. https://doi.org/10.1016/j.earscirev.2018.05.001.

Dong, Y.P., He, D.F., Sun, S.S., Liu, X.M., Zhou, X.H., Zhang, F.F., Yang, Z., Cheng, B., Zhao, G.C., Li, J.H., 2018. Subduction and accretionary tectonics of the East Kunlun Orogen, western segment of the Central China Orogenic System. Earth-Sci. Rev. 186, 231–261. https://doi.org/10.1016/j.earscirev.2017.12.006.

Dong, Y.P., Sun, S.S., Santosh, M., Hui, B., Sun, J.P., Zhang, F.F., Cheng, B., Yang, Z., Shi, X.H., He, D.F., Cheng, C., Liu, X.M., Zhou, X.H., Wang, W., Qi, N., 2022. Cross Orogenic Belts in Central China: Implications for the tectonic and paleogeographic evolution of the East Asian continental collage. Gondwana Res. 109, 18–88. https://doi.org/10.1016/j.gr.2022.04.012.

Duan, H.W., 2014. Characteristics and metallogenic regularities of porphyry ore deposit, eastern section of East Kunlun Mountains. Master Thesis, China University of Geosciences (Beijing), p. 103 (in Chinese with English abstract).

Fan, X.Z., Sun, F.Y., Xu, C.H., Wu, D.Q., Yu, L., Wang, L., Yan, C., Bakht, S., 2022. Volcanic rocks of the Elashan Formation in the Dulan-Xiangride Basin, East Kunlun Orogenic Belt, NW China: Petrogenesis and implications for Late Triassic geodynamic evolution. Int. Geol. Rev. 64 (9), 1270–1293. https://doi.org/10.1080/00206814.2021.1923074.

Feng, C.Y., Li, D.S., Qu, W.J., Du, A.D., Wang, S., Su, S.S., Jiang, J.H., 2009. Re-Os isotopic dating of molybdenite from the Suolajier Skarn type copper-molybdenite deposit of Qimantag mountain in Qinghai province and its geological significance. Rock Miner. Anal. 28 (03), 223–227 (in Chinese with English abstract).

Feng, C.Y., Li, D.S., Wu, Z.S., Li, J.H., Zhang, Z.Y., Zhang, A.K., Shu, X.F., Su, S.S., 2010. Major types, time-space distribution and metallogenies of polymetallic deposits in the Qimantage metallogenic belt, Eastern Kunlun area. Northwestern Geol. 43 (04), 10–17 (in Chinese with English abstract).

Feng, C.Y., Wang, X.P., Shu, X.F., Zhang, A.K., Xiao, Y., Liu, J.N., Ma, S.C., Li, G.C., Li, D. X., 2011a. Isotopic chronology of the Hutouya Skarn lead-zinc polymetallic ore district in Qimantagh area of Qinghai Provience and Its geological significance. J. Jilin Univ. (Earth Sci. Ed.) 41 (06), 1806–1817 (in Chinese with English abstract).

Feng, C.Y., Ma, S.C., Li, G.C., Wang, S., Shu, X.F., 2011b. Diagenetic and metallogenic chronology constraints on the genesis of Jingren-Yingqinggou polymetallic deposit. Qinghai Province. J. Mineral. Petrol. 31 (S1), 576–577 (in Chinese with English abstract).

Feng, C.Y., 2002. Multiple orogenic processes and mineralization of orogenic gold deposits in the East Kunlun Orogen, Qinghai Province. Ph.D. Thesis, Chinese Academy of Geological Sciences (Institute of Mineral Resources) (in Chinese with English abstract).

Franklin, J.M., Gibson, L., Jonasson, I., Galley, A., 2005. Volcanogenic massive sulfide deposits. In: Hedenquist, J.W., Thompson, J.F.H., Goldfarb, R.J., Richards, J.P. (Eds.), Economic Geology: One Hundredth Anniversary Volume 1905–2005. Society of Economic Geologists, Littleton, pp. 523–560.

Fu, C.L., Yan, Z., Guo, X.Q., Niu, M.L., Chen, L., Xia, W.J., 2016. Magma source and tectonic setting of the granitoids associated with Saishitang Cu deposit in the West Qinling terrane. Acta Petrol. Sin. 32 (7), 1997–2014 (in Chinese with English abstract).

Gao, Y.B., Li, W.Y., Ma, X.G., Zhang, Z.W., Tang, Q.Y., 2012. Genesis, geochronology and Hf isotopic compositions of magmatic rocks in Galinge iron deposit, East Kunlun. J. Lanzhou Univ. 48 (02), 36–47 (in Chinese with English abstract).

Gao, Y.B., Li, K., Qian, B., Li, W.Y., Li, D.S., Su, S.S., Zhang, C.G., Zhang, D.M., Wang, S. M., 2015. The genesis of granodiorites and dark enclaves from the Kaerqueka deposit in East Kunlun Belt: evidence from zircon U-Pb dating, geochemistry and Sr-Nd-Hf isotopic compositions. Geol. China 42 (03), 646–662 (in Chinese with English abstract).

Gao, Y.B., Li, K., Qian, B., Li, W.Y., He, S.Y., Zhang, D.M., Wang, S.M., 2018. The metallogenic chronology of Kaerqueka deposit in Eastern Kunlun: evidences from molybdenite Re-Os and phlogopite Ar-Ar ages. Geotecton. Metallog. 42 (01), 96–107 (in Chinese with English abstract).

Gao, H.C., Sun, F.Y., Li, B.L., Qian, Y., Wang, L., Zhang, Y.J., 2020. Geochronological and geochemical constraints on the origin of the Hutouya polymetallic skarn deposit in the East Kunlun Orogenic Belt, NW China. Minerals 10 (12), 1136. https://doi.org/10.3390/min10121136.

Goldfarb, R.J., Baker, T., Dubé, B., Groves, D.I., Gosselin, P., 2005. Distribution, character, and genesis of gold deposits in metamorphic terranes. Econ. Geol. 100th Anniversary, 407–450.

Griffin, W.L., Wang, X., Jackson, S.E., Pearson, N.J., O'Reilly, S.Y., Xu, X., Zhou, X., 2002. Zircon chemistry and magma mixing, SE China: in-situ analysis of Hf isotopes, Tonglu and Pingtan igneous complexes. Lithos 61 (3), 237–269. https://doi.org/10.1016/S0024-4937(02)00082-8.

Groves, D.I., Goldfarb, R.J., Gebre-Mariam, M., Hagemann, S.G., Robert, F., 1998. Orogenic gold deposits: a proposed classification in the context of their crustal distribution and relationship to other gold deposit types. Ore Geol. Rev. 13 (1–5), 7–27. https://doi.org/10.1016/S0169-1368(97)00012-7.

Groves, D.I., Condie, K.C., Goldfarb, R.J., Hronsky, J., Vielreicher, R.M., 2005. 100th Anniversary Special Paper: secular changes in global tectonic processes and their influence on the temporal distribution of gold-bearing mineral deposits. Econ. Geol. 100 (2), 203–224. https://doi.org/10.2113/100.2.203.

Groves, D.I., Santosh, M., 2021. Craton and thick lithosphere margins: the sites of giant mineral deposits and mineral provinces. Gondwana Res. 100, 195–222. https://doi.org/10.1016/j.gr.2020.06.008.

Guo, X.Z., 2020. The intermediate-acid magmatism and polymetallic mineralization in East Kunlun, Paleo-Tethys. Ph.D. Thesis, China University of Geosciences, p. 246 (in Chinese with English abstract).

Guo, X.Z., Xie, W.H., Zhou, H.B., Tian, C.S., Li, J.C., Kong, H.L., Yang, T., Yao, X.G., Jia, Q. Z., 2019. Zircon U-Pb chronology and geochemistry of rhyolite porphyry in Nagengkangqieer sliver polymetallic deposit, East Kunlun and their geological significance. Earth Sci. (J. China Univ. Geosci.) 44 (7), 2505–2518 (in Chinese with English abstract).

Guo, X.Z., Jia, Q.Z., Lü, X.B., Li, J.C., Kong, H.L., Yao, X.G., 2020. The Permian Sn metallogenic event and its geodynamic setting in East Kunlun, NW China: evidence from zircon and cassiterite geochronology, geochemistry, and Sr–Nd–Hf isotopes of the Xiaowolong skarn Sn deposit. Ore Geol. Rev 118, 103370. https://doi.org/10.1016/j.oregeorev.2020.103370.

Guo, X.Z., Zhou, T.F., Jia, Q.Z., Li, J.C., Kong, H.L., 2022. Highly differentiated felsic granites linked to Mo mineralization in the East Kunlun Orogenic Belt, NW China: constrains from geochemistry, and Sr-Nd-Hf isotopes of the Duolongqiarou porphyry Mo deposit.. Ore Geol. Rev. 145, 104891. https://doi.org/10.1016/j.oregeorev.2022.104891.

Han, J.J., Li, Y.D., Song, C.Z., He, J., Han, X., Qi, C.W., 2020. Zircon U-Pb dating and geochemistry of granite in the Reshui area of Dulan county, eastern section of East Kunlun Orogen and its tectonic implications. Acta Geol. Sin. 94 (3), 768–781 (in Chinese with English abstract).
He, D.F., Dong, Y.P., Zhang, F.F., Yang, Z., Sun, S.S., Cheng, B., Zhou, B., Liu, X.M., 2016. The 1.0 Ga S–type granite in the East Kunlun Orogen, Northern Tibetan Plateau: implications for the Meso - to Neoproterozoic tectonic evolution. J. Asian Earth Sci. 130, 46–59. https://doi.org/10.1016/j.jseaes.2016.07.019.
Hou, Z.Q., Zaw, K., Pan, G.T., Mo, X.X., Xu, Q., Hu, Y.Z., Li, X.Z., 2007. Sanjiang Tethyan metallogenesis in S.W. China: tectonic setting, metallogenic epochs and deposit types. Ore Geol. Rev. 31 (1–4), 48–87. https://doi.org/10.1016/j.oregeorev.2004.12.007.
Hou, Z.Q., Zhang, H.R., 2015. Geodynamics and metallogeny of the eastern Tethyan metallogenic domain. Ore Geol. Rev. 70, 346–384. https://doi.org/10.1016/j.oregeorev.2014.10.026.
Hou, Z.Q., Duan, L.F., Lu, Y.J., Zheng, Y.C., Di Cheng, Z., Ming, Y.Z., Yang, Z.S., Di, W.B., Ru, P.Y., Dan, Z.Z., McCuaig, T.C., 2015. Lithospheric architecture of the Lhasa Terrane and its control on ore deposits in the Himalayan-Tibetan Orogen. Econ. Geol. 110 (6), 1541–1575. https://doi.org/10.2113/econgeo.110.6.1541.
Hu, F.Y., Ducea, M.N., Liu, S.W., Chapman, J.B., 2017. Quantifying crustal thickness in continental collisional belts: global perspective and a geologic application. Sci. Rep. 7, 7058. https://doi.org/10.1038/s41598-017-07849-7.
Hu, Y., Niu, Y.L., Li, J.Y., Ye, L., Kong, J.J., Chen, S., Zhang, Y., Zhang, G.R., 2016. Petrogenesis and tectonic significance of the late Triassic mafic dikes and felsic volcanic rocks in the East Kunlun Orogenic Belt, Northern Tibet Plateau. Lithos 245, 205–222. https://doi.org/10.1016/j.lithos.2015.05.004.
Huang, H., Niu, Y.L., Nowell, G., Zhao, Z.D., Yu, X.H., Zhu, D.C., Mo, X.X., Ding, S., 2014. Geochemical constraints on the petrogenesis of granitoids in the East Kunlun Orogenic Belt, northern Tibetan Plateau: implications for continental crust growth through syn-collisional felsic magmatism. Chem. Geol. 370, 1–18. https://doi.org/10.1016/j.chemgeo.2014.01.010.
Huang, X.K., Wei, J.H., Li, H., Chen, M.T., Wang, Y.L., Li, G.M., Yan, M.Q., Zhang, X.M., 2021. Zircon U-Pb geochronological, elemental and Sr-Nd-Hf isotopic constraints on petrogenesis of the Late Triassic quartz diorite in Balong region, East Kunlun Orogen. Earth Sci. 46 (06), 2037–2056 (in Chinese with English abstract).
Kemp, A.I.S., Hawkesworth, C.J., Paterson, B.A., Kinny, P.D., 2006. Episodic growth of the Gondwana supercontinent from hafnium and oxygen isotopes in zircon. Nature 439 (7076), 580–583. https://doi.org/10.1038/nature04505.
King, P.L., White, A., Chappell, B.W., Allen, C.M., 1997. Characterization and origin of aluminous A-type granites from the Lachlan Fold Belt, Southeastern Australia. J. Petrol. 38 (3), 371–391. https://doi.org/10.1093/petroj/38.3.371.
Le Bas, M.J., Le Maitre, R.W., Streckeisen, A., Zanettin, B.A., Iugs, s.o.t.s., 1986. Chemical classification of volcanic rocks based on the total alkali-silica diagram. J. Petrol. 27 (3), 745–750. https://doi.org/10.1093/petrology/27.3.745.
Leach, D.L., Sangster, D.F., Kelley, K.D., Large, R.R., Walters, S.G., 2005. Sediment-hosted lead-zinc deposits: A global perspective. Society of Economic Geologists, Littleton, Colorado, pp. 561–607.
Li, J.C., 2017. Metallogenic regularity and metallogenic prognosis of gold deposit in the East Kunlun Orogen, Qinghai province. Ph.D. Thesis, Chang'an University (in Chinese with English abstract).
Li, N., Chen, Y., Santosh, M., Pirajno, F., 2015b. Compositional polarity of Triassic granitoids in the Qinling Orogen, China: implication for termination of the northernmost paleo-Tethys. Gondwana Res. 27 (1), 244–257. https://doi.org/10.1016/j.gr.2013.09.017.
Li, X.K., Chen, J., Wang, R.C., Li, C., 2018b. Temporal and spatial variations of Late Mesozoic granitoids in the SW Qiangtang, Tibet: implications for crustal architecture, Meso-Tethyan evolution and regional mineralization. Earth-Sci. Rev. 185, 374–396. https://doi.org/10.1016/j.earscirev.2018.04.005.
Li, J.C., Guo, X.Z., Kong, H.L., Yao, X.G., Jia, Q.Z., 2021. Geochronology, geochemical characteristics and geological significance of A-Type granite from the Lalangmai area, East Kunlun. Acta Geol. Sin. 95 (05), 1508–1522 (in Chinese with English abstract).
Li, R.B., Pei, X.Z., Li, Z.C., Liu, Z.Q., Chen, G.C., Chen, Y.X., Wei, F.H., Gao, J.M., Liu, C.J., Pei, L., 2012. Geological characteristics of Late Paleozoic-Mesozoic unconformities and their response to some significant tectonic events in eastern part of Eastern Kunlun. Earth Sci. Front. 19 (5), 244–254 (in Chinese with English abstract).
Li, R.B., Pei, X.Z., Pei, L., Li, Z.C., Chen, G.C., Chen, Y.X., Liu, C.J., Wang, M., 2018a. The Early Triassic Andean-type Halagatu granitoids pluton in the East Kunlun orogen, northern Tibet Plateau: response to the northward subduction of the Paleo-Tethys Ocean. Gondwana Res. 62, 212–226. https://doi.org/10.1016/j.gr.2018.03.005.
Li, H.R., Qian, Y., Sun, F.Y., Li, L., 2020. Geochemistry, zircon geochronology, and isotopic systematics of the Zhanbuzhale granites in the East Kunlun, Qinghai Province, Northwestern China: implications for the tectonic setting. Can. J. Earth Sci. 57 (2), 275–291. https://doi.org/10.1139/cjes-2018-0251.
Li, B.L., Zhi, Y.B., Zhang, L., Ding, Q.F., Xu, Q.L., Zhang, Y.J., Qian, Y., Wang, G., Peng, B., Ao, C., 2015a. U-Pb dating, geochemistry, and Sr-Nd isotopic composition of a granodiorite porphyry from the Jiadanggen Cu-(Mo) deposit in the Eastern Kunlun metallogenic belt, Qinghai Province, China. Ore Geol. Rev. 67, 1–10. https://doi.org/10.1016/j.oregeorev.2014.11.008.
Liang, G.Z., Yang, K.F., Sun, W.Q., Fan, H.R., Li, X.H., Lan, T.G., Hu, H.L., Chen, Y.W., 2021. Multistage ore-forming processes and metal source recorded in texture and composition of pyrite from the Late Triassic Asiha gold deposit, Eastern Kunlun Orogenic Belt, western China. J. Asian Earth Sci. 220, 104920. https://doi.org/10.1016/j.jseaes.2021.104920.
Liu, J.N., Feng, C.Y., Qi, F., Li, G.C., Ma, S.C., Xiao, Y., 2012. SIMS zircon U-Pb dating and fluid inclusion studies of Xiadeboli Cu-Mo ore district in Dulan county, Qinghai Province, China. Acta Petrol. Sin. 28 (02), 679–690 (in Chinese with English abstract).
Liu, J.N., Feng, C.Y., He, S., Pei, R.F., Li, D.X., Ju, H.Y., Bai, S.L., 2017b. Zircon U-Pb and phlogopite Ar-Ar ages of the monzogranite from Yemaquan iron-zinc deposit in Qinghai Province. Geotecton. Metallog. 41 (06), 1158–1170 (in Chinese with English abstract).
Liu, B., Ma, C.Q., Huang, J., Wang, L.X., Zhao, S.Q., Yan, R., Sun, Y., Xiong, F.H., 2017a. Petrogenesis and tectonic implications of Upper Triassic appinite dykes in the East Kunlun Orogenic Belt, Northern Tibetan Plateau. Lithos 284–285, 766–778. https://doi.org/10.1016/j.lithos.2017.05.016.
Liu, Y.H., Mo, X.X., Yu, X.H., Zhang, X.T., Xu, G.W., 2006. Zircon SHRIMP U-Pb dating of Jingren granite, Yemaquan region of East Kunlun and its geological significance. Acta Petrol. Sin. 10, 2457–2463 (in Chinese with English abstract).
Lu, H.F., Yang, Y.Q., He, J., Li, J.Q., 2017. Zircon U-Pb age dating for granodiorite porphyry and molybdenite Re-Os isotope dating of Halongxiuma molybdenite (tungsten) deposit in the East Kunlun area and its geological significance. J. Mineral. Petrol. 37 (02), 33–39 (in Chinese with English abstract).
Lydon, J.W., 1988. Ore deposit models. 14. Volcanogenic massive sulphide deposits part 2: genetic models. Geosci. Can. 15 (1), 43–65.
Maniar, P.D., Piccoli, P.M., 1989. Tectonic discrimination of granitoids. Geol. Soc. Am. Bull. 101(5), 635-643.
Mi, X.M., 2019. Geological features and potential analysis of ore prospecting at adjacent area in Yazigou. Master Thesis, Lanzhou University, 92 pp. (in Chinese with English abstract).
Mo, X.X., Luo, Z.H., Deng, J.F., Yu, X.H., Liu, C.D., Chen, H.W., Yuan, W.M., Liu, Y.H., 2007. Granitoids and crustal growth in the East-Kunlun Orogenic Belt. Geol. J. China Univ. 03, 403–414 (in Chinese with English abstract).
Mole, D.R., Fiorentini, M.L., Thebaud, N., Cassidy, K.F., McCuaig, T.C., Kirkland, C.L., Romano, S.S., Doublier, M.P., Belousova, E.A., Barnes, S.J., Miller, J., 2014. Archean komatiite volcanism controlled by the evolution of early continents. Proc. Natl. Acad. Sci. U.S.A. 111 (28), 10083–10088. https://doi.org/10.1073/pnas.1400273111.
Mole, D.R., Kirkland, C.L., Fiorentini, M.L., Barnes, S.J., Cassidy, K.F., Isaac, C., Belousova, E.A., Hartnady, M., Thebaud, N., 2019. Time-space evolution of an Archean craton: a Hf-isotope window into continent formation. Earth-Sci. Rev. 196, 102831. https://doi.org/10.1016/j.earscirev.2019.04.003.
Morishita, Y., Nakano, T., 2008. Role of basement in epithermal deposits: the Kushikino and Hishikari gold deposits, southwestern Japan. Ore Geol. Rev. 34 (4), 597–609. https://doi.org/10.1016/j.oregeorev.2008.09.009.
Pan, Z.C., Sun, F.Y., Cong, Z.C., Tian, N., Xin, W., Wang, L., Zhang, Y.J., Wu, D.Q., 2022. Petrogenesis and tectonic implications of the Triassic granitoids in the Ela Mountain area of the East Kunlun Orogenic Belt. Minerals (Basel) 12 (880), 880. https://doi.org/10.3390/min12070880.
Pan, G.T., Wang, L.Q., Li, R.S., Yuan, S.H., Ji, W.H., Yin, F.G., Zhang, W.P., Wang, B.D., 2012. Tectonic evolution of the Qinghai-Tibet Plateau. J. Asian Earth Sci. 53, 3–14. https://doi.org/10.1016/j.jseaes.2011.12.018.
Peccerillo, A., Taylor, S.R., 1976. Geochemistry of Eocene calc-alkaline volcanic rocks from the Kastamonu area, northern Turkey. Contrib. Mineral. Petrol. 58 (1), 63–81. https://doi.org/10.1007/BF00384745.
Peng, B., Li, B., Zhao, T.F., Wang, C., Chang, J.J., Wang, G.Z., Yang, W.L., 2017. Identification of A-type granite in the southeastern Kunlun Orogen, Qinghai Province, China: implications for the tectonic framework of the Eastern Kunlun Orogen. Geol. J. 52 (3), 454–469. https://doi.org/10.1002/gj.2775.
Qu, H.Y., Friehauf, K., Santosh, M., Pei, R.F., Li, D.X., Liu, J.N., Zhou, S.M., Wang, H., 2019. Middle-Late Triassic magmatism in the Hutouya Fe–Cu–Pb–Zn deposit, East Kunlun Orogenic Belt, NW China: implications for geodynamic setting and polymetallic mineralization. Ore Geol. Rev. 113, 103088. https://doi.org/10.1016/j.oregeorev.2019.103088.
Ratschbacher, L., Hacker, B.R., Calvert, A., Webb, L.E., Grimmer, J.C., McWilliams, M. O., Ireland, T., Dong, S., Hu, J., 2003. Tectonics of the Qinling (Central China): tectonostratigraphy, geochronology, and deformation history. Tectonophysics 366 (1), 1–53. https://doi.org/10.1016/S0040-1951(03)00053-2.
Richards, J.P., 2015. Tectonic, magmatic, and metallogenic evolution of the Tethyan orogen: from subduction to collision. Ore Geol. Rev. 70, 323–345. https://doi.org/10.1016/j.oregeorev.2014.11.009.
Roy, S.K., Kumar, M.R., Srinagesh, D., 2014. Upper and lower mantle anisotropy inferred from comprehensive SKS and SKKS splitting measurements from India. Earth Planet. Sci. Lett. 392, 192–206. https://doi.org/10.1016/j.epsl.2014.02.012.
Santosh, M., Groves, D.I., 2022. Global metallogeny in relation to secular evolution of the Earth and supercontinent cycles. Gondwana Res. 107, 395–422. https://doi.org/10.1016/j.gr.2022.04.007.
Shao, F.L., Niu, Y.L., Liu, Y., Chen, S., Kong, J.J., Duan, M., 2017. Petrogenesis of Triassic granitoids in the East Kunlun Orogenic Belt, northern Tibetan Plateau and their tectonic implications. Lithos 282, 33–44. https://doi.org/10.1016/j.lithos.2017.03.002.
Shi, C., Li, R.S., He, S.P., Ji, W.H., Gu, P.Y., Chen, S.J., Zhang, H.D., 2017. A study of the ore-forming age of the Hutouya deposit and its geological significance: geochemistry and U-Pb zircon ages of biotite monzonitic granite in Qimantag, East Kunlun Mountains. Geol. Bull. China 36 (06), 977–986 (in Chinese with English abstract).

Sillitoe, R.H., 2008. Special Paper: Major Gold Deposits and Belts of the North and South American Cordillera: Distribution, Tectonomagmatic Settings, and Metallogenic Considerations. Econ. Geol. 103 (4), 663–687. https://doi.org/10.2113/gsecongeo.103.4.663.

Sillitoe, R.H., 2010. Porphyry copper systems. Econ. Geol. 105 (1), 3–41. https://doi.org/10.2113/gsecongeo.105.1.3.

Sun, S.S., McDonough, W.F., Saunders, A.D., Norry, M.J., 1989. Chemical and isotopic systematics of oceanic basalts; implications for mantle composition and processes. Geol. Soc. Spec. Publ. 42 (1), 313–345. https://doi.org/10.1144/GSL.SP.1989.042.01.19.

Tesauro, M., Kaban, M.K., Petrunin, A.G., El Khrepy, S., Al-Arifi, N., 2018. Strength and elastic thickness variations in the Arabian Plate: a combination of temperature, composition and strain rates of the lithosphere. Tectonophysics 746, 398–411. https://doi.org/10.1016/j.tecto.2017.03.004.

Thomas, C., Billen, M.I., 2009. Mantle transition zone structure along a profile in the SW Pacific: thermal and compositional variations. Geophys. J. Int. 176(1), 113-125. https://doi.org/10.1111/j.1365-246X.2008.03934.x.

Turner, D.R., Bowman, J.R., 1993. Origin and evolution of skarn fluids, empire zinc skarns, central mining district, NEW-MEXICO, USA. Appl. Geochem. 8 (1), 9–36. https://doi.org/10.1016/0883-2927(93)90054-K.

Wang, C.M., Bagas, L., Lu, Y.J., Santosh, M., Du, B., McCuaig, T.C., 2016a. Terrane boundary and spatio-temporal distribution of ore deposits in the Sanjiang Tethyan Orogen: insights from zircon Hf-isotopic mapping. Earth-Sci. Rev. 156, 39–65. https://doi.org/10.1016/j.earscirev.2016.02.008.

Wang, F.C., Chen, J., Xie, Z.Y., Li, S.P., Tan, S.X., Zhang, Y.B., Wang, T., 2013. Geological features and Re-Os isotopic dating of the Lalingzaohuo molybdenum polymetallic deposit in East Kunlun. Geol. China 40 (04), 1209–1217 (in Chinese with English abstract).

Wang, C.M., Deng, J., Bagas, L., Wang, Q., 2017a. Zircon Hf–isotopic mapping for understanding crustal architecture and metallogenesis in the Eastern Qinling Orogen. Gondwana Res. 50, 293–310. https://doi.org/10.1016/j.gr.2017.04.008.

Wang, H., Feng, C.Y., Li, D.X., Li, C., Ding, T.Z., Liao, F.Z., 2016b. Geology, geochronology and geochemistry of the Saishitang Cu deposit, East Kunlun Mountains, NW China: constraints on ore genesis and tectonic setting. Ore Geol. Rev. 72, 43–59. https://doi.org/10.1016/j.oregeorev.2015.07.002.

Wang, Y.B., Guo, Y.P., Zeng, Q.D., Guo, L.X., 2018. Petrogenesis and tectonic setting of the Shiduolong skarn Pb-Zn deposit in the East Kunlun Orogenic Belt: constraints from whole-rock geochemical, zircon U-Pb and Hf isotope analyses. Geol. J. 53 (3), 1022–1038. https://doi.org/10.1002/gj.2941.

Wang, C.Y., Ma, Z.Y., Zhou, Q.L., Ma, C.X., Ma, Q., Qi, Y.Q., 2017b. Rock geochemical characteristics and tectonic environment analysis of Cu-Mo polymetallic mining area of Qingshui River ore district, Eastern Kunlun, Qinghai province. J. Qinghai Univ. 05, 73–81 (in Chinese with English abstract).

Wang, X.X., Wang, T., Ke, C.H., Yang, Y., Li, J.B., Li, Y.H., Qi, Q.J., Lv, X.Q., 2015. Nd–Hf isotopic mapping of Late Mesozoic granitoids in the East Qinling orogen, central China: constraint on the basements of terranes and distribution of Mo mineralization. J. Asian Earth Sci. 103, 169–183. https://doi.org/10.1016/j.jseaes.2014.07.002.

Wang, X.Y., Zhu, X.Y., Li, J.D., Wang, Y.W., Jiang, B.B., Wu, J.R., Huang, X.K., Zhao, Z.Y., Ábalos, B., 2021. Two stage magmatism and their skarn-type mineralization in the Niukutou ore district, Qinghai Province. Acta Petrol. Sin. 37 (05), 1567–1586 (in Chinese with English abstract).

Webb, M., White, L.T., Manning, C.J., Jost, B.M., Tiranda, H., 2020. Isotopic mapping reveals the location of crustal fragments along a long-lived convergent plate boundary. Lithos, 372–373, 105687. https: 10.1016/j.lithos.2020.105687.

Whalen, J.B., Currie, K.L., Chappell, B.W., 1987. A-type granites: geochemical characteristics, discrimination and petrogenesis. Contrib. Mineral. Petrol. 95 (4), 407–419. https://doi.org/10.1007/BF00402202.

Wu, C., Chen, H., Lu, Y., 2021a. Crustal structure control on porphyry copper systems in accretionary orogens: insights from Nd isotopic mapping in the Central Asian Orogenic Belt. Mineral. Deposita 57, 631–641. https://doi.org/10.1007/s00126-021-01074-z.

Wu, Z.N., Ji, W.H., He, S.P., Chen, S.J., Yu, P.S., Shi, C., Chen, F.N., Zhang, H.S., Peng, Y., 2015. LA-ICP-MS zircon U-Pb dating and geochemical characteristics of granodiorite in Rilonggou area, Xinghai County, Qinghai Province. Geol. Bull. China 34 (09), 1677–1688 (in Chinese with English abstract).

Wu, F.Y., Yang, Y.H., Xie, L.W., Yang, J.H., Xu, P., 2006. Hf isotopic compositions of the standard zircons and baddeleyites used in U-Pb geochronology. Chem. Geol. 234 (1–2), 105–126. https://doi.org/10.1016/j.chemgeo.2006.05.003.

Wu, J.J., Zeng, Q.D., Santosh, M., Fan, H.R., Wei, Z.H., Yang, K.F., Zhang, Z.M., Li, X.H., Liang, G.Z., 2021c. Intrusion-related orogenic gold deposit in the East Kunlun belt, NW China: a multiproxy investigation. Ore Geol. Rev. 139, 104550. https://doi.org/10.1016/j.oregeorev.2021.104550.

Wu, C., Zuza, A.V., Chen, X.H., Ding, L., Levy, D.A., Liu, C.F., Liu, W.C., Jiang, T., Stockli, D.F., 2019. Tectonics of the Eastern Kunlun Range: cenozoic reactivation of a paleozoic-early mesozoic orogen. Tectonics 38 (5), 1609–1650. https://doi.org/10.1029/2018TC005370.

Wu, C., Li, J., Zuza, A.V., Haproff, P.J., Chen, X.H., Ding, L., 2021b. Proterozoic−Phanerozoic tectonic evolution of the Qilian Shan and Eastern Kunlun Range, northern Tibet. GSA Bull. 134 (9–10), 2179–2205. https://doi.org/10.1130/B36306.1.

Xia, R., 2017. Paleo-Tethys Orogenic process and gold metallogenesis of East Kunlun. Ph.D. Thesis, China University of Geosciences (Beijing), p. 215 (in Chinese with English abstract).

Xia, R., Wang, C.M., Deng, J., Carranza, E.J.M., Li, W.L., Qing, M., 2014. Crustal thickening prior to 220 Ma in the East Kunlun Orogenic Belt: insights from the Late Triassic granitoids in the Xiao-Nuomuhong pluton. J. Asian Earth Sci. 93, 193–210. https://doi.org/10.1016/j.jseaes.2014.07.013.

Xia, R., Deng, J., Qing, M., Li, W.L., Guo, X.D., Zeng, G.Z., 2017. Petrogenesis of ca. 240 Ma intermediate and felsic intrusions in the Nan' getan: implications for crust–mantle interaction and geodynamic process of the East Kunlun Orogen. Ore Geol. Rev. 90, 1099–1117. https://doi.org/10.1016/j.oregeorev.2017.04.002.

Xiao, Y., Feng, C.Y., Liu, J.N., Yu, M., Zhou, J.H., Li, D.X., Zhao, Y.M., 2013. LA-ICP-MS zircon U-Pb dating and sulfur isotope characteristics of Kendekeke Fe-polymetallic deposit, Qinghai province. Miner. Deposits 32 (01), 177–186 (in Chinese with English abstract).

Xiong, F.H., 2014. Spatial-temporal pattern, petrogenesis and geological implications of Paleo-Tethyan granitoids in the East Kunlun Orogenic Belt. Ph.D. Thesis, China University of Geosciences, p. 191 (in Chinese with English abstract).

Xiong, F.H., Ma, C.Q., Zhang, J.Y., Liu, B., 2012. The origin of mafic microgranular enclaves and their host granodiorites from East Kunlun, Northern Qinghai-Tibet Plateau: implications for magma mixing during subduction of Paleo-Tethyan lithosphere. Mineral. Petrol. 104 (3–4), 211–224. https://doi.org/10.1007/s00710-011-0187-1.

Xiong, F.H., Ma, C.Q., Jiang, H.A., Zhang, H., 2016. Geochronology and petrogenesis of Triassic high-K calc-alkaline granodiorites in the East Kunlun Orogen, West China: Juvenile lower crustal melting during post-collisional extension. J. Earth Sci. 27 (3), 474–490. https://doi.org/10.1007/s12583-016-0674-6.

Xiong, F.H., Ma, C.Q., Chen, B., Ducea, M.N., Hou, M.C., Ni, S.J., 2019. Intermediate-mafic dikes in the East Kunlun Orogen, Northern Tibetan Plateau: a window into paleo-arc magma feeding system. Lithos 340–341, 152–165. https://doi.org/10.1016/j.lithos.2019.05.012.

Xu, Q.L., 2014. Study on metallogenesis of porphyry deposits in Eastern Kunlun Orogenic Belt, Qinghai Province. Ph.D. Thesis, Jilin University, p. 208 (in Chinese with English abstract).

Xue, H.R., Sun, F.Y., Li, L., Xin, W., 2020. Geochronology, geochemistry, and Sr-Nd-Hf isotopes of the Late Permian-Early Triassic granitoids in Eastern Kunlun Orogen, Northwest China: petrogenesis and implications for geodynamic setting. Int. Geol. Rev. 63 (6), 696–716. https://doi.org/10.1080/00206814.2020.1722968.

Yang, Y.Q., Li, B.L., Ma, Y.J., Tan, Y., Bao, S.B., Li, J.T., Yu, X.L., Wang, J.Y., 2018. Geochemistry and genesis of monzonitic granite from Aikengdelesite area in East Kunlun, Qinghai. Northwestern Geol. 51 (01), 104–114 (in Chinese with English abstract).

Yang, T., 2015. Geological characteristics and genesis discussion of the Tawenchahanxi Fe-polymetallic deposit in Qimantage area, Qinghai province. Master Thesis, Chang' an University, 92 pp. (in Chinese with English abstract).

Yao, L., Lü, Z.C., Zhao, C.S., Pang, Z.S., Yu, X.F., Yang, T., Li, Y.S., Liu, P., Zhang, M.C., 2017. Zircon U-Pb geochronological, trace element, and Hf isotopic constraints on the genesis of the Fe and Cu skarn deposits in the Qiman Tagh area, Qinghai Province, Eastern Kunlun Orogen, China. Ore Geol. Rev. 91, 387–403. https://doi.org/10.1016/j.oregeorev.2017.09.017.

Yu, M., Feng, C.Y., Santosh, M., Mao, J.W., Zhu, Y.F., Zhao, Y.M., Li, D.X., Li, B., 2017. The Qiman Tagh Orogen as a window to the crustal evolution in northern Qinghai-Tibet Plateau. Earth-Sci. Rev. 167, 103–123. https://doi.org/10.1016/j.earscirev.2017.02.008.

Yu, M., Dick, J.M., Feng, C., Li, B., Wang, H., 2020. The tectonic evolution of the East Kunlun Orogen, northern Tibetan Plateau: a critical review with an integrated geodynamic model. J. Asian Earth Sci. 191, 104168. https://doi.org/10.1016/j.jseaes.2019.104168.

Zhang, A.K., 2012. Studies on late Paleozoic-early Mesozoic magmatism and mineralization in Yemaquan area, Qinghai province. Ph.D. Thesis, China University of Geosciences (Beijing), p. 166 (in Chinese with English abstract).

Zhang, B.L., 2013. Study on the Geochemical Characteristics and Metallogenic Age of Balugou Polymetallic Deposits in Dulan County, Qinghai Province. Master Thesis, Jilin University, p. 81 (in Chinese with English abstract).

Zhang, X.F., Li, Z.M., Jia, Q.Z., Song, Z.B., Chen, X.Y., Zhang, Y.L., Li, D.S., Shu, X.F., 2016b. Geochronology, geochemistry and geological significance of granite porphyry in Hutouya polymetallic deposit, Qimantage area, Qinghai Province. J. Jilin Univ. (Earth Sci. Ed.) 46 (03), 749–765 (in Chinese with English abstract).

Zhang, J.Y., Ma, C.Q., Li, J.W., Pan, Y.M., 2017. A possible genetic relationship between orogenic gold mineralization and post-collisional magmatism in the eastern Kunlun Orogen, western China. Ore Geol. Rev. 81, 342–357. https://doi.org/10.1016/j.oregeorev.2016.11.003.

Zhang, W., Zhou, H.W., Zhu, Y.H., Mao, W.L., Tong, X., Ma, Z.Q., Cao, Y.L., 2016a. The evolution of Triassic granites associated with mineralization within East Kunlun Orogenic Belt: evidence from petrology, geochemistry and zircon U-Pb geochronology of the Mohexiala pluton. Earth Sci. 41 (08), 1334–1348 (in Chinese with English abstract).

Zhao, X., Wei, J.H., Fu, L.B., Huizenga, J.M., Santosh, M., Chen, J.J., Wang, D.Z., Li, A.B., 2020. Multi-stage crustal melting from Late Permian back-arc extension through Middle Triassic continental collision to Late Triassic post-collisional extension in the East Kunlun Orogen. Lithos 360-361, 105446. https://doi.org/10.1016/j.lithos.2020.105446.

Zhao, X., Fu, L.B., Wei, J.H., Bagas, L., Santosh, M., Liu, Y., Zhang, D.H., Zhou, H.Z., 2019. Late Permian back-arc extension of the eastern Paleo-Tethys Ocean:

evidence from the East Kunlun Orogen, Northern Tibetan Plateau. Lithos 340–341, 34–48. https://doi.org/10.1016/j.lithos.2019.05.006.
Zhao, X., Fu, L.B., Santosh, M., Wei, J.H., Chen, J.J., 2022. The growth and evolution of continental crust contributed by multiple sources in the East Kunlun Orogen during Early Paleozoic. Earth-Sci. Rev. 233, 104190. https://doi.org/10.1016/j.earscirev.2022.104190.
Zhong, S.H., Li, S.Z., Feng, C.Y., Liu, Y.J., Santosh, M., He, S.Y., Qu, H.Y., Liu, G.Y., Seltmann, R., Lai, Z.Q., Wang, X.H., Song, Y.X., Zhou, J., 2021. Porphyry copper and skarn fertility of the northern Qinghai-Tibet Plateau collisional granitoids. Earth-Sci. Rev. 214, 103524. https://doi.org/10.1016/j.earscirev.2021.103524.
Zhou, H.Z., 2019. Indosinian magmatic evolution and copper polymetallic mineralization in the Erashan area, Qinghai Province. Ph.D. Thesis, China University of Geosciences, p. 266 (in Chinese with English abstract).
Zhou, H.Z., Zhang, D.H., Wei, J.H., Wang, D.Z., Santosh, M., Shi, W.J., Chen, J.J., Zhao, X., 2020. Petrogenesis of Late Triassic mafic enclaves and host granodiorite in the Eastern Kunlun Orogenic Belt, China: implications for the reworking of juvenile crust by delamination-induced asthenosphere upwelling. Gondwana Res. 84, 52–70. https://doi.org/10.1016/j.gr.2020.02.012.
Zhu, R.Z., Lai, S.C., Qin, J.F., Zhao, S.W., Santosh, M., 2018b. Strongly peraluminous fractionated S-type granites in the Baoshan Block, SW China: implications for two-stage melting of fertile continental materials following the closure of Bangong-Nujiang Tethys. Lithos 316–317, 178–198. https://doi.org/10.1016/j.lithos.2018.07.016.
Zhu, Y.X., Wang, L.X., Ma, C.Q., He, Z.X., Deng, X., Tian, Y., 2022. Petrogenesis and tectonic implication of the Late Triassic A1-type alkaline volcanics from the Xiangride area, eastern segment of the East Kunlun Orogen (China). Lithos 412–413, 106595. https://doi.org/10.1016/j.lithos.2022.106595.
Zhu, D.Q., Zhu, H.B., Li, B.L., Li, H.Y., Li, G.T., 2018a. Re-Os geochronology of molybdenite from Reshui Cu-Mo deposit in Dulan, Qinghai and its geological significance. Glob. Geol. 37 (04), 1004–1017 (in Chinese with English abstract).